How does precipitation data influence the land surface data assimilation for drought monitoring?

Keyhan Gavahi*, Peyman Abbaszadeh, Hamid Moradkhani

Department of Civil, Construction and Environmental Engineering, Center for Complex Hydrosystems Research

University of Alabama, Tuscaloosa, AL, USA

*Corresponding author: kgavahi@crimson.ua.edu

Abstract

Droughts are among the costliest natural hazards that occur annually worldwide. Their socioeconomic impacts are significant and widespread, affecting the sustainable development of human societies. This study investigates the influence of different forcing precipitation data in driving Land Surface Models (LSMs) and characterizing drought conditions. Here, we utilize our recently developed LSM data assimilation system for probabilistically monitoring drought over the Contiguous United States (CONUS). The Noah-MP LSM model is forced with two widely used precipitation data including IMERG (Integrated Multi-satellitE Retrievals for GPM) and NLDAS (North American Land Data Assimilation System). Soil moisture and evapotranspiration are known to have a strong relationship in the land-atmospheric interaction processes. Unlike other studies that attempted the individual assimilation of these variables, here we propose a multivariate data assimilation framework. Therefore, in both modeling scenarios, the data assimilation approach is used to integrate remotely sensed MODIS (Moderate Resolution Imaging Spectroradiometer) evapotranspiration and SMAP (Soil Moisture Active Passive) soil moisture observations into the Noah-MP LSM. The results of this study indicate that the source of precipitation data has a significant impact on the performance of LSM data assimilation system for drought monitoring. The findings revealed that NLDAS and IMERG precipitation can result in a significant difference in identifying drought severity depending on the region and time of the year. Furthermore, our analysis indicates that regardless of the precipitation forcing data product used in the land surface data assimilation system, our modeling framework can effectively detect the drought impacts on crop yield. Additionally, we calculated the drought probability based on the ensemble of soil moisture percentiles and found that there exist temporal and spatial discrepancies in drought probability maps generated from the NLDAS and IMERG precipitation forcings.

Keywords: Bayesian methods; Data assimilation; Ensembles; Precipitation; Land surface model

1. Introduction

Drought is among the costliest natural hazards with significant socio-economic impact that causes billions of dollars damage in agriculture sector, among others every year (Sheffield et al., 2014a). Scientists all around the world have raised concerns about droughts and their vast impacts on the environment, hydrology, ecology, and agriculture (Baniya et al., 2019; Chen et al., 2020; Huang et al., 2018; Javed et al., 2021; Koohi et al., 2021; Nichol and Abbas, 2015; Zhao et al., 2018). Furthermore, studies have shown that the frequency and intensity of extreme events such as droughts are increasing under global warming, threatening the stability and sustainable development of the ecosystem and economy (Heim, 2002; Liu et al., 2016; Nijssen et al., 2014; Svoboda et al., 2002) According to the U.S. Federal Emergency Management Agency (FEMA), the U.S. experiences droughts almost every year causing $6-8 billion of damage annually (FEMA, 1995). To name a few examples, the North American drought in 1988 resulted in nearly $62 billion in losses (Cook et al., 2007). The 2012 flash drought which covered most of the central U.S. caused an intense reduction in crop productions and led to about $12 billion in agricultural loss (Jin et al., 2019). In 2020, the western US drought caused about $13 billion in damages (NOAA, 2021a).

Drought is a multifaceted phenomenon classified into four major types including agricultural, meteorological, hydrological, and socioeconomic drought each focusing on different aspects of adverse effects of this hazard. Among the various adverse impacts, the influence of droughts on the agricultural sector is the most direct and significant. The global economic losses due to the impacts of drought on the agricultural sector account for more than 50% of total losses due to all meteorological disasters (Baniya et al., 2019; Liu et al., 2016; Sheffield et al., 2014b) Hence, improving drought early warning systems (DEWS) and agricultural drought monitoring and forecasting capabilities are imperative to mitigate its devastating impacts.. The U.S. Drought Monitoring system (USDM) provides drought monitoring maps over the Contiguous U.S. on a weekly basis. The National Oceanic and Atmospheric Administration (NOAA) was authorized by congress in 2006 to develop National Integrated Drought Information System (NIDIS). NIDIS's main goal is to provide an integrated national drought monitoring and forecasting system at federal, state, and local levels (NIDIS, 2021). All these ongoing efforts are to ensure the support for improvements in monitoring, forecasting, and communication to mitigate the adverse effects of droughts especially on the agricultural sector.

Agricultural drought refers to a predefined period with an excessive deficit in soil moisture (SM) which could ultimately result in crop failure (Araneda-Cabrera et al., 2021; Liu et al., 2018). Accurate estimation of soil moisture is imperative for agricultural drought monitoring and developing early warning systems to reduce crop yield loss. For this purpose, several drought indices have been developed based on stand-alone or combination of variables including precipitation, temperature, evapotranspiration (ET), and soil moisture itself (Barbu et al., 2014; Gavahi et al., 2020; Hain et al., 2012; Kimwatu et al., 2021; Vicente-Serrano et al., 2010).

SM and ET have the potential to be indirectly assimilated into the land surface model (LSM) to achieve a more accurate and reliable estimation of these prognostic variables (Hain et al., 2012; Kumar et al., 2014; Sawada et al., 2015; Zhan et al., 2021). However, soil moisture predictions by the LSMs are prone to considerable uncertainty mainly due to uncertainty in meteorological forcing, in particular precipitation (Zeng et al., 2021). The main reason for this can be attributed to the high level of spatiotemporal variability of forcing data. Additionally, these uncertainties are magnified by spatiotemporal variabilities of land-surface processes such as exchanges of energy, mass, and momentum. Hence, characterization of uncertainty in model states, parameters, and forcings are vital to improving model predictions especially for dynamic systems sensitive to initial conditions (Cheng et al., 2020; Khaki et al., 2020; Piazzi et al., 2021). Data assimilation (DA) provides a robust framework for integrating observations with LSMs to improve the model predictive skills and provide a more accurate estimation of water and energy balance computations (Cosgrove et al., 2003; Sawada et al., 2015; Zhou et al., 2020). The main objective of DA is to exploit the most recently available information provided by real-time observations to improve model forecasts (Moradkhani et al., 2018). Furthermore, DA merges the past and current observations by utilizing the model's prognostic equations to provide a more reliable and accurate estimation of the model's states and parameters while accounting for various sources of uncertainties in modeling (Abbaszadeh et al., 2019a; Moradkhani et al., 2018). However, the effectiveness of DA is highly dependent on the choice of variables to assimilate and their spatiotemporal correlations (Gavahi et al., 2020).

The significance of uncertainties stemming from the forcing data can not be underestimated, especially precipitation, which is the most erroneous meteorological forcing in land surface modeling and soil moisture estimation. More accurate precipitation estimations at fine spatial and temporal resolutions have proven to improve our land surface hydrological simulations and provide us with a more accurate representation of extreme events such as floods and droughts (Lai et al., 2019; Liu et al., 2020; Scofield and Kuligowski, 2003). A wide range of precipitation products is available through weather radars, rain gauge stations, satellite-based estimates, and numerical-based estimates (Hazra et al., 2019). Each of these can have variable accuracies across spatio-temporal scales and thus result in different representations of extreme events such as drought. It is well-known that satellite-based precipitation estimations are inherently prone to complex uncertainties at high spatiotemporal scales (Hossain and

Anagnostou, 2005). These uncertainties will propagate through model simulations and will influence the land-surface interaction processes and consequently affect the simulated SM (Shrestha et al., 2020). This will in turn affect the agricultural drought monitoring which is mainly based on SM predictions and consequently, different drought conditions are estimated given the uncertainty in precipitation forcing. Similarly, accurate impact assessment of agricultural drought on crop loss is highly dependent on the accuracy and reliability of drought maps that are developed based on predicted SM. For example, the characterization of a flash drought is heavily affected by the precipitation data uncertainty that is propagated through different layers in the modeling processes. This affects the antecedent soil moisture conditions prior to the onset of flash drought (Yuan et al., 2019). Hence, in this study, we aim to comprehensively investigate the suitability of two precipitation products as inputs to a multivariate data assimilation framework that uses Noah-MP as its LSM and examines the impacts for different applications such as crop yield loss, onset and termination of flash droughts, and probabilistic drought maps over the CONUS. We use the multivariate fully parallelized divide-and-conquer evolutionary particle filter algorithm developed by (Gavahi et al., 2020) as the data assimilation framework in which SM and ET are simultaneously assimilated into the Noah-MP model for more accurate and reliable SM predictions. It should also be noted that the main objective of this study is not to suggest which precipitation product, e.g., NLDAS or IMERG, is superior for agricultural drought monitoring purpose, rather to reveal the extent of differences when different precipitation datasets are used. Are they small enough to be negligible, or in some areas, the results are completely different in terms of existence of a drought condition and/or its severity.

The remainder of the paper is organized as follows. Section 2 describes the datasets used. Section 3 provides a brief explanation of the Noah-MP land surface model. In section 4 the methodology for parallel joint data assimilation procedure is briefly described and section 5 discusses the results. Finally, section 6 summarizes the findings of this study, its limitations, and future works.

2. Datasets

2.1 SMAP Soil Moisture Products

In January 2015, the National Aeronautics and Space Administration (NASA) launched the Soil Moisture Active Passive (SMAP) satellite to provide soil moisture estimates at the global scale. The satellite uses brightness temperature through two active (radar sensor at 3-km resolution) and passive (radiometer at 36-km resolution) sensors to estimate the surface soil moisture. The active sensor provides more information due to its fine spatial resolution, but it is more prone to uncertainties due to sensitivity to vegetation cover and its swath width. Unfortunately, three months after the launch of the SMAP satellite its radar instrument failed and became non-operational and the radiometer sensor is the only operational sensor since then, providing soil moisture estimates at 36-km spatial resolution. Later on, NASA released an enhanced version of the SMAP product. In this new version, using the Backus–Gilbert optimal interpolation algorithm, the SMAP soil moisture at 36-km resolution is downscaled to the 9-km grid spacing (Das et al., 2018).

Although SMAP provides important SM information for global applications, its usefulness for local studies such as irrigation management and planning, flood forecasting, crop production, and agricultural drought monitoring is in question due to its coarse resolution. To cope with this issue, we used an ensemble-based machine learning approach to downscale the SMAP soil moisture from its native 36-km resolution to the fine resolution of 1-km while incorporating geophysical and atmospheric information gathered from high-resolution remote sensing data and gauged observations. For a more detailed explanation of the proposed downscaling method, we refer the interested readers to the (Abbaszadeh et al., 2019b). Also, a comprehensive validation analysis using the most reliable in-situ soil moisture observations across the CONUS was provided by Abbaszadeh et al., (2021). Therefore, in this study, we have used the downscaled SMAP soil moisture product at the 1-km spatial resolution to be assimilated into the Noah-MP land surface model. The dataset is publicly available over the CONUS and can be accessed via https://moradkhani.ua.edu/smap.

2.2 NLDAS Forcing data

Phase 2 of the North American Land Data Assimilation System (NLDAS-2) has been used in this study as the meteorological forcing data (Xia et al., 2012). To support modeling endeavors, NLDAS provides high-quality forcing data that are spatiotemporally consistent and validated against the best available observations (Xia et al., 2012). This dataset covers data from 1979 to present at 1 hour temporal and ~12.5km spatial resolution. In this study, the Noah-MP land surface model is forced by total precipitation, incoming longwave and shortwave radiation, atmospheric pressure, vapor pressure, air temperature, and wind speed. In this study, the hourly NLDAS-2 meteorological forcing data at ~12.5km spatial resolution from 2016 through 2020 was used to force the Noah-MP land surface model. Also, the climatology of precipitation over the CONUS was created using this dataset from 2000 through 2020. The dataset is publicly available and can be accessed through (NLDAS, 2021).

2.3 IMERG precipitation

As part of the Global Precipitation Measurement (GPM) program, NASA developed the Integrated Multi-satellite Retrievals for GPM (IMERG) (Tan et al., 2019). The IMERG algorithm uses the CMORPH motion vector method to incorporate the microwave-derived precipitation measurements. However, in its final version, version 06, the total precipitable water vapor field gathered from numerical models is used to compute the motion vectors instead of the geostationary infrared (Geo-IR) imagery (Guilloteau et al., 2021). Additionally, IMERG assimilates the infrared precipitation measurements from the PERSIANN-CCS (Precipitation Estimation from Remotely Sensed Information using Artificial Neural Networks–Cloud Classification System) (Hong et al., 2004) using the Kalman filtering assimilation method. The IMERG algorithm is run twice and provides three products with different latency. The so-called Early product uses only forward morphing (by using a one-way Kalman filter approach) and is available ~4 hours after the observation. The Late product uses both forward and backward morphing (using a two-way Kalman smoother) with a ~14-hour latency. The Final product also uses forward and backward morphing and is available after the monthly ground-based observations analysis are received and hence can be accessed ~3.5 months after the observation month. All three products have a spatial resolution of 0.1 degrees. In this study, the calibrated daily precipitation measurements at ~10km spatial resolution for the period of 2016 through 2020 is obtained from the final product (IMERG-F) that includes the gauge adjustments and used as one of the meteorological forcings of the Noah-MP model. Also, the climatology of the precipitation over the CONUS was created using the IMERG-F from 2000 through 2020.

2.4 MODIS evapotranspiration (ET)

The MOD16 evapotranspiration product from MODIS was used for ET assimilation. This product provides global evapotranspiration at 8-day, monthly and annual intervals with a 1-km spatial resolution (Mu et al., 2011, 2007). Considering the temporal and spatial scale mismatches between MODIS and SMAP datasets, various scenarios for the DA can be devised. For example, the SMAP SM assimilation can be performed at a daily time scale, and then the MODIS ET is assimilated every 8 days. Another scenario could be filtering the maps with the day of the year (DOY) map provided with the MODIS ET product to create daily maps of ET. Here, we used the first approach for ET assimilation. Hence, here we used the DOY map of the MODIS ET product with 1-km spatial resolution from 2016 through 2020.

3. Noah-MP land surface model

The Noah-MP LSM uses a series of options for its land-atmospheric interaction processes. Noah-MP is the enhanced version of the Noah land surface model with improved physics and multi-parameterization options (Niu et al., 2011). The improvements include but are not limited to a multi-layer snowpack, an interactive vegetation canopy, and a dynamic ground water component. Users are provided with different choices of parameterization in runoff modeling, canopy stomatal resistance, leaf dynamic, groundwater modeling, and soil moisture (Cai et al., 2014). More specifically the vegetation canopy has been significantly improved by adding a distinct vegetation canopy layer that is defined by several key features such as crown radius, orientation, density, and radiometric parameters. Unlike the Noah model that used a table of prescribed monthly values for vegetation properties, the dynamic vegetation model of the Noah-MP is capable of predicting the leaf area index (LAI) and green vegetation fractions (Salamanca et al., 2018).

4. Methodology

4.1 Data Assimilation

The data assimilation method in this study utilizes sequential Monte Carlo techniques to generate replicas of model forcing and states and then through a formal Bayesian approach obtains a full probability distribution of the variables of interests and characterizes the predictive uncertainty. The sequential assimilation techniques have been widely used in hydrological prediction studies (Moradkhani et al., 2018). The method provides an effective means to merge ground-based and remotely sensed observations with an LSM. In this study, we use the Evolutionary Particle Filter with Markov Chain Monte Carlo (hereafter EPFM) to improve the Noah-MP model predictions and account for the associated uncertainties (Abbaszadeh et al., 2018). The effectiveness and usefulness of this approach for drought monitoring was recently discussed in some studies (Gavahi et al., 2020). Here, we briefly explain the EPFM data assimilation technique.

4.2 Sequential Bayesian Theory

A nonlinear dynamic system that has Spatio-temporal variability can be described using equations 1 and 2 (Moradkhani et al., 2018).

$$x_t = f(x_{t-1}, u_t, \theta) + \omega_t \qquad (1)$$

$$y_t = h(x_t) + v_t \qquad (2)$$

In these equations $x_t \in \mathbb{R}^n$ represents the vector of uncertain state variables and the uncertain forcing data at time step t is shown by u_t. θ and y_t represent the vector of model parameters and observation data, respectively. ω_t represents model structural error and υ_t is the observation error. According to the Bayesian theory, the posterior distribution of state variables at time t can be approximated using the following equations:

$$p(x_t|y_{1:t}) = p(x_t|y_{1:t-1}, y_t) = \frac{p(y_t|x_t)p(x_t|y_{1:t-1})}{p(y_t|y_{1:t-1})} = \frac{p(y_t|x_t)p(x_t|y_{1:t-1})}{\int p(y_t|x_t)p(x_t|y_{1:t-1})dx_t} \qquad (3)$$

$$p(x_t|y_{1:t-1}) = \int p(x_t, x_{t-1}|y_{1:t-1})dx_{t-1} = \int p(x_t|x_{t-1})p(x_{t-1}|y_{1:t-1})dx_{t-1} \qquad (4)$$

where $p(y_t|x_t)$ denotes the likelihood at time step t and $p(x_t|y_{1:t-1})$ represents the prior distribution. $p(y_t|y_{1:t-1})$ and $p(y_{1:t})$ are the normalization factor and the marginal likelihood function, respectively and both of these can be approximated as follows:

$$p(y_{1:t}) = p(y_1)\prod p(y_t|y_{1:t-1}) \qquad (5)$$

$$p(y_t|y_{1:t-1}) = \int p(y_t, x_t|y_{1:t-1})dx_t = \int p(y_t|x_t)p(x_t|y_{1:t-1})dx_t \qquad (6)$$

Solving equation (3) analytically is only possible for special cases (i.e. linear systems), hence this formula is usually approximated using a set of random samples.

4.3 Evolutionary Particle Filter with MCMC (EPFM)

The PF-MCMC is a successor version of PF-SIR that combines the Markov Chain Monte Carlo (MCMC) with the Particle Filter (PF) (Moradkhani et al., 2012). In this approach, Equation (3) can be approximated using the following equation:

$$p(x_t|y_{1:t}) \approx \sum_{i=1}^{N} w^{i+}\delta\left(x_t - x_t^i\right) \qquad (7)$$

where w^{i+} represents the posterior weight of the i-th particle. δ is the Dirac delta function and N denotes the number of particles. Therefore, the normalized weights can be calculated as follows:

$$w^{i+} = \frac{w^{i-}.\,p\left(y_t\middle|x_t^i, \theta_t^i\right)}{\sum_{i=1}^{N} w^{i-}.\,p\left(y_t\middle|x_t^i, \theta_t^i\right)} \qquad (8)$$

In this equation 8, w^{i-} represents the prior weight of the i-th particle and $p\left(y_t\middle|x_t^i, \theta_t^i\right)$ is calculated using the likelihood $L\left(y_t\middle|x_t^i, \theta_t^i\right)$ in the following equation:

$$L\left(y_t|x_t^i, \theta_t^i\right) = \frac{1}{\sqrt{(2\pi)^m |R_t|}} exp\left[-\frac{1}{2}\left(y_t - h\left(x_t^i\right)\right)^T {R_t}^{-1}\left(y_t - h\left(x_t^i\right)\right)\right] \qquad (9)$$

After that, having the posterior weights, the state variables and parameters are resampled using the SIR. Afterward, the proposal parameter distribution is created as follows:

$$\theta_t^{i,p} = \theta_t^{i+} + \varepsilon_t^i \qquad \varepsilon_t^i \sim N\left[0, s_t Var\left(\theta_t^{i-}\right)\right] \qquad (10)$$

In equation 10, θ_t^{i-} and θ_t^{i+} represent the parameters before and after SIR calculations. s_t denotes a small tuning factor while $\theta_t^{i,p}$ is the proposal parameter samples. To accept or reject $\theta_t^{i,p}$, a metropolis acceptance ratio α is determined as follows:

$$\alpha = \min\left(1, \frac{p\left(x_t^{i,p}, \theta_t^{i,p}\middle|y_{1:t}\right)}{p\left(x_t^{i+}, \theta_t^{i+}\middle|y_{1:t}\right)}\right) \qquad (11)$$

In which $p\left(x_t^{i,p}, \theta_t^{i,p}\middle|y_{1:t}\right)$ is the proposed joint probability distribution:

$$p\left(x_t^{i,p}, \theta_t^{i,p}\middle|y_{1:t}\right) \propto p\left(y_{1:t}\middle|x_t^{i,p}, \theta_t^{i,p}\right).\,p\left(x_t^{i,p}\middle|\theta_t^{i,p}, y_{1:t-1}\right).\,p\left(\theta_t^{i,p}\middle|y_{1:t-1}\right) \qquad (12)$$

$$x_t^{i,p} = f\left(x_{t-1}^{i+}, u_t^{i+}, \theta_t^{i,p}\right) \tag{13}$$

In which $x_t^{i,p}$ and u_t^{i+} denote a sample from the state proposal distribution and the resampled forcing data at time step t, respectively while s_t represents a time-variant unknown variable that can be determined using the Variable Variance Multiplier (VVM) method (Abbaszadeh et al., 2019a).

The EPFM is an extension of PF-MCMC which utilizes the MCMC approach twice in a sequential framework. First, the MCMC is used for the crossover and mutation procedures embedded in the EPFM algorithm to produce a more comprehensive prior distribution for state variables. Then, MCMC is utilized for the second time after the resampling procedure to generate the proposal parameter distribution. The main advantage of the EPFM algorithm is that it significantly impedes particle degeneracy and sample impoverishment which are two major issues in using the particle filter method. For a more detailed explanation of this approach, we refer the interested readers to (Abbaszadeh et al., 2018).

4.4 Parallelization scheme

One of the main challenges in applying the particle filter data assimilation schemes is the computational burden. Although a great portion of this computational complexity stems from the model, an efficient implementation of the algorithm is necessary to avoid domination of the run-time by the assimilation part. To this excerpt, in our previous study, we have developed a fully parallelized divide-and-conquer algorithm that incorporates both model and domain decomposition efficiently (Gavahi et al., 2020). The algorithm recursively partitions the model domain into smaller portions and performs the EPFM calculations such as crossover, mutation, kernel density estimation, and likelihood function evaluation on each portion. After that, it will gather the final results from each portion and merge them to provide the final computations on the entire domain. This approach will significantly improve the framework performance and makes it possible to apply the framework to a larger domain such as the entire CONUS in this study. For more information on the details of the algorithm, we refer the interested readers to (Gavahi et al., 2020).

5. Results and Discussion

5.1 Comparison between NLDAS and IMERG

Figure 1 shows a comparison between monthly precipitation anomalies for IMERG and NLDAS data for the year 2020. For the most part in the year 2020, precipitation has been less than normal especially for the west of CONUS according to both datasets. The climatology is for the period of 2000-2020, consistent with the period of IMERG precipitation product. The overall patterns are similar but the intensities are different. On average IMERG is showing higher precipitation anomalies than NLDAS especially for the months of Jan – Apr over the east and southeastern of CONUS. The IMERG precipitation patterns are generally smoother than the NLDAS. One reason for this can be that NLDAS is a model-based product whereas the IMERG is a merged product of various satellite and ground-based measurement sources. The highest precipitation anomalies are present in months of Jan – Apr across the Pacific Northwest as well as portions of the central and southern CONUS. The higher differences between IMERG and NLDAS can also be observed for the same period across these areas. This is also consistent with the National Climate Reports of NOAA (NOAA, 2021b) in which much-above-average wetness was reported. This shows that IMERG and NLDAS precipitation datasets have differences in their precipitation climatology which can impose a direct effect on the SM climatology used for agricultural drought monitoring.

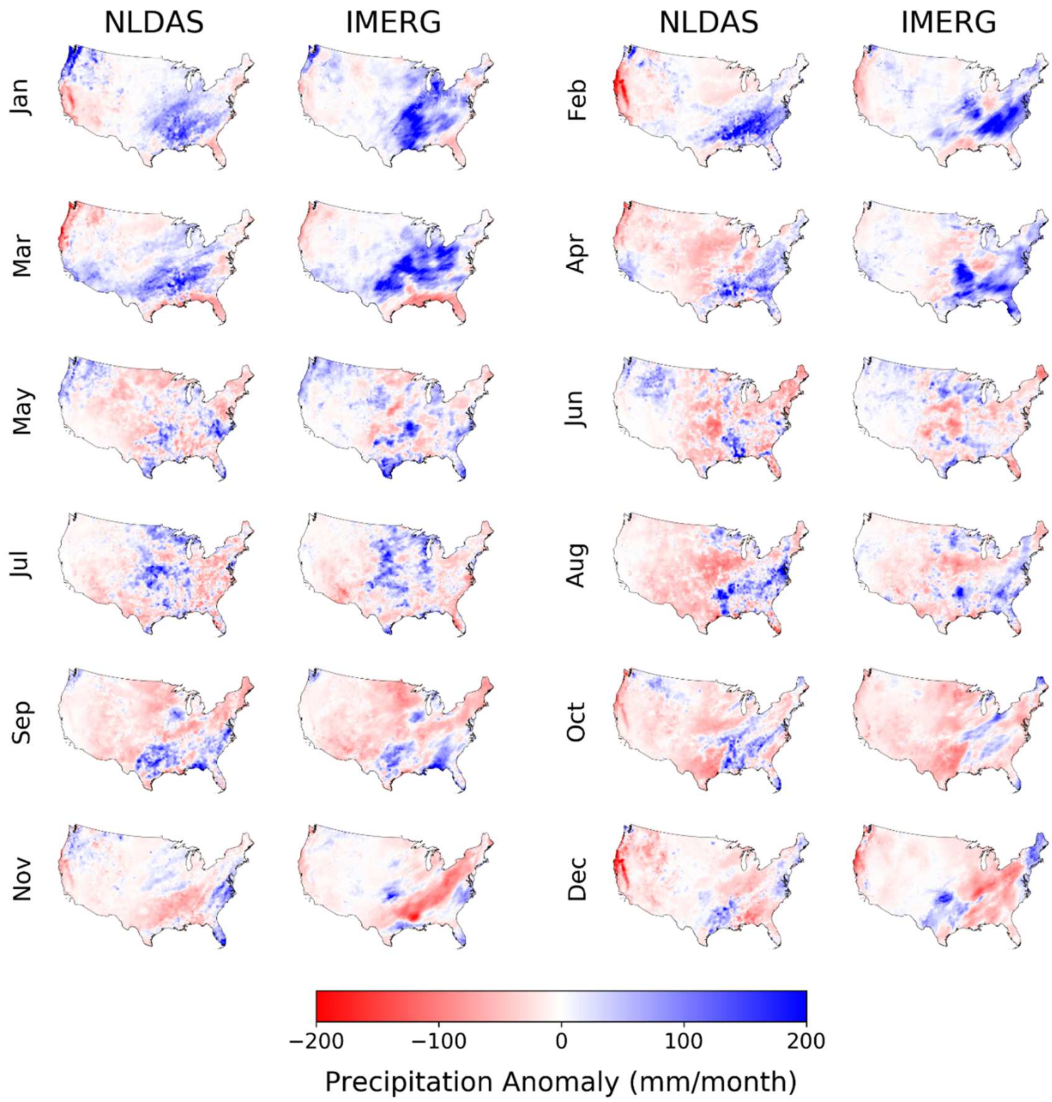

Figure 1. Comparison between monthly precipitation anomalies for IMERG and NLDAS data for the year 2020.

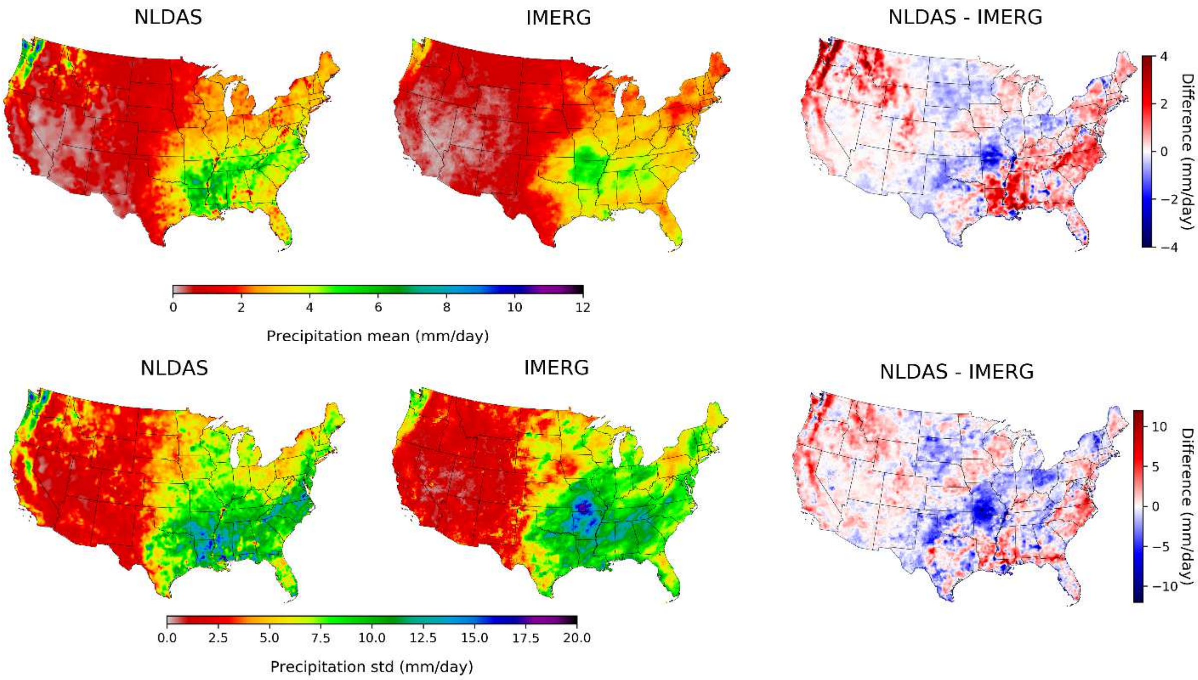

Figure 2. Comparison between precipitation mean and standard deviation of IMERG and NLDAS for the 2000-2020 period.

The highest discrepancy between IMERG and NLDAS is observed across the rain-fed regions such as the Pacific Northwest and the southeast US. As seen in Figure 2, the NLDAS has higher precipitation mean and slightly lower standard deviation as compared to the IMERG. However, over the central US and especially in Arkansas and Missouri states, unlike the NLDAS, IMERG shows higher mean and standard deviation. The lowest rate of precipitation can be observed in the west and southwest of the US where the difference between IMERG and NLDAS is at its minimum.

5.2 Drought monitoring over the CONUS

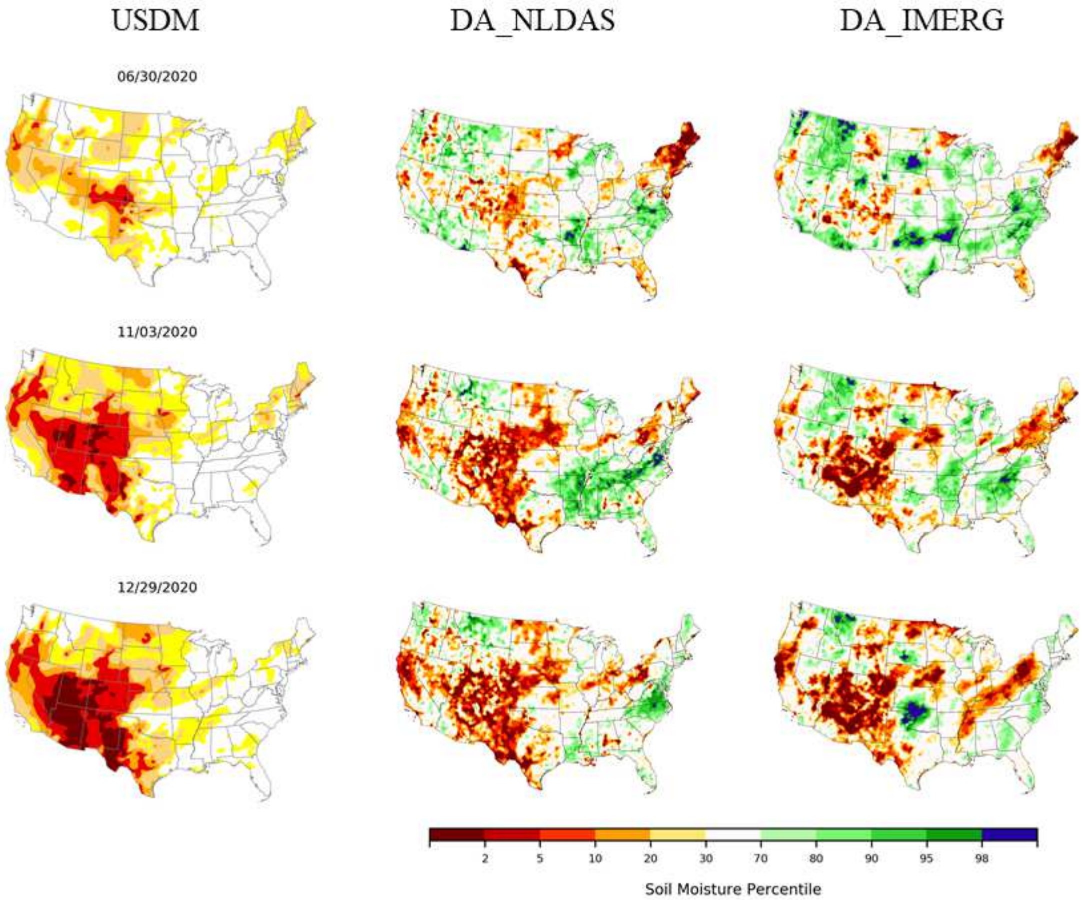

Figure 3. Weekly agricultural drought maps (based on root zone SM) generated from DA results forced with IMERG (DA_IMERG) and NLDAS (DA_NLDAS) for three different dates in 2020. The USDM maps have also been provided for comparison. The day June 2nd, 2020 shown in the first row means the weekly drought conditions beginning on June 2nd, 2020, and ending on June 8th, 2020 the same with USDM.

The USDM depicts drought conditions by classifying it into five categories: abnormally dry for percentiles below 30% (D0), moderate drought for percentiles ≤ 20% (D1), severe drought for percentiles ≤ 10% (D2), extreme drought for percentiles ≤ 5% (D3), and finally exceptional drought for percentile ≤

2% (D4). Here, DA_IMERG, and DA_NLDAS refer to drought maps (based on root zone SM) generated using IMERG and NLDAS data, respectively. Based on the USDM map, in June 2020, D1 (moderate) to D2 (severe) drought conditions extended from the West Coast to Rocky Mountains and into the High Plains. A comparison with both NLDAS and IMERG maps in Figure 3 shows that most of these areas are in normal conditions except for some small areas in the north of California for both IMERG and NLDAS and small patches of D2 to D3 categories in Oregon. The IMERG and NLDAS results both agree with VIC modeled total soil moisture (NCDC, 2021a) CPC (NCDC, 2021b) and NLDAS ensemble-mean Soil Moisture Percentile (SMP) (NCDC, 2021c). However, the IMERG is showing a wetter condition with a smaller drought extent. The main reason for the discrepancies with the USDM map may be due to the lack of consideration of groundwater. Both USGS observations (NCDC, 2021d) and NASA GRACE-based shallow groundwater drought indicator (NCDC, 2021e) show low groundwater estimates for the West Coast to Rocky mountains. Another interesting observation is in Florida where both IMERG and NLDAS results agree on some patches with D2 to D3 drought whereas the USDM map is showing a completely normal condition. Similarly, this can be attributed to the groundwater estimates as USDM Real-Time Groundwater Level Network shows much above normal conditions (NCDC, 2021d). Apart from that, normal to low-level evapotranspiration has been observed for most of the West Coast area according to 1-month EDDI (NCDC, 2021f) and ESI (NCDC, 2021g). This could be another reason for showing a smaller drought extent by the multivariate DA framework in which ET and SM are assimilated into the model. Abnormally dry conditions can be observed in sothern to central high plains and moderate drought in northern plains based on the USDM map. The NLDAS results to some extent agree with the USDM especially in the west of Texas whereas the IMERG results are showing a completely normal condition for this area. It is interesting to note that the drought maps from SPoRT LIS (NCDC, 2021h), VIC (NCDC, 2021a) and NLDAS (NCDC, 2021c) agree with those from the USDM and DA_NLDAS while the CPC drought map (NCDC, 2021b) is more consistent with that of DA_IMERG.

The drought conditions exacerbated in October while moderate to extreme drought with some areas of exceptional drought (D4) extended from the West Coast to Rocky Mountains and well into the adjacent high plains according to the USDM map (NCEI, 2020). Both DA_IMERG and DA_NLDAS show similar drought extent over the entire US except for the west coast where the DA_NLDAS results in less drought coverage (similar to USDM) compared to the DA_IMERG where the area is almost drought-free. Drought maps from VIC (NCDC, 2021i) and CPC (NCDC, 2021j) are more consistent with those of USDM whereas the NLDAS ensemble-mean (NCDC, 2021k) represents drought similar to that of DA_NLDAS. The most interesting state is Montana where USDM, DA_NLDAS, and DA_IMERG reveal different drought conditions. USDM exhibits moderate to severe drought conditions across the entire state. While DA_NLDAS shows mostly wet conditions, however, for DA_IMERG the eastern and western Montana are represented by wet and dry conditions, respectively. Furthermore, VIC, CPC, and NLDAS ensemble-mean show normal to wet conditions for this state, while NASA GRACE root zone soil moisture (NCDC, 2021l) reports highly wet conditions. It is important to note that while all the drought declarations report no drought condition for Montana state, the USDM shows otherwise.

As it is shown earlier in Figure 1 below-normal monthly precipitation continued in November and December which resulted in intensification and expansion of the drought condition in December. Warmer than normal temperatures were also present in this month

(NCDC, 2021m). Altogether it resulted in drought expansion in the northern and southern Plains. D1 to D4 drought categories covered most of the central to northern Plains and drought expanded in some areas of the southern Plains. One interesting observation is the West Coast regions (i.e., California and Arizona). According to USDM maps, D2 to D3 drought categories is covering most of this region whereas drought maps from DA_NLDAS and DA_IMERG show normal conditions. This result corroborates with GRACE root-zone soil moisture (NCDC, 2021n) while CPC (CPC, 2021), NLDAS, and VIC are more consistent with the USDM map. Further investigation also showed that DA_IMERG reports a D2 to D4 drought condition across the Ozark-Quachita-Appalachian Forests (OQAF) ecoregion, while two other products (USDM and DA_NLDAS) are representing only a slight drought extent over the northern part. The IMERG precipitation anomaly shown in Figure 1 also shows up to 150 mm below normal precipitation for the OQAF region which is not as intense in NLDAS precipitation (with up to 50 mm anomaly). This shows the significance of precipitation data uncertainty which greatly affects the model results.

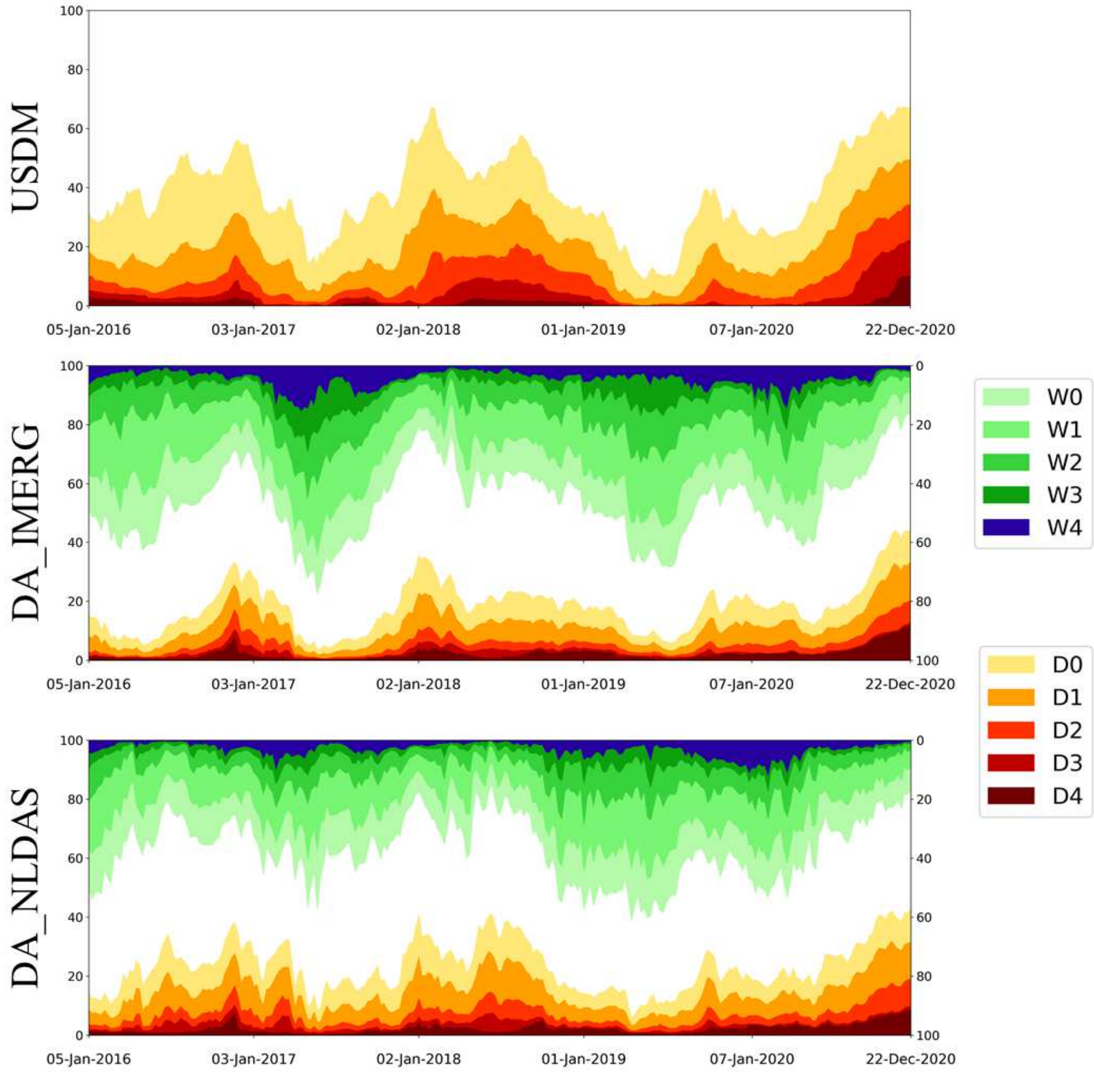

Figure 4. The drought extent from Jan 2016 to the end of 2020 estimated by USDM, DA_NLDAS, and DA_IMERG. The wetness conditions are also shown for DA_NLDAS and DA_IMERG results.

A comparison of the drought extent between USDM, DA_NLDAS, and DA_IMERG is shown in Figure 4 to examine the temporal variations and consistencies between products. On the second y-axis for the DA_NLDAS and DA_IMERG, the wetness is also shown to provide a more comprehensive picture of similarities and differences between these two. Both products are showing strong temporal consistencies with the USDM with correlation coefficients higher than

0.70 for D0 to D3 categories. As it can be seen in this figure and based on the results in Table 1, the extent of drought from DA_NLDAS is more correlated with those from USDM for abnormally-, moderate- and severe drought conditions (i.e., D0 to D2 categories) whereas the drought extent of DA_IMERG is showing higher correlations with that of USDM for extreme- and exceptional drought conditions (i.e., D3 and D4 categories). This implies depending on the severity of drought conditions, different meteorological forcing observations may result in different drought characterization. From Table 1, we also noticed that DA_IMERG and DA_NLDAS are more consistent on the dry side with higher correlation coefficients compared to the wet side. One plausible reason behind this is that droughts mostly occur during the absence of precipitation, and NLDAS and IMERG products are similarly representing no-precipitation areas. Further analysis also shows that the USDM extent of drought is much higher than both DA_IMERG and DA_NLDAS. This may be related to the procedure that USDM adopts to polygonize the drought extent, which is different from the method we applied in this study.

Several drought hotspots have been depicted by the USDM, such as in November 2016, February 2018, and August 2018. As it is shown in this figure the temporal drought hotspots detected by the DA_NLDAS and DA_IMERG agree well with those of USDM, although the intensities are different. While in August 2018 both USDM and DA_NLDAS are showing a big spike of drought extent, the DA_IMERG remains relatively stable until February 2019. It should also be noted that although the temporal variations of drought coverages from all three products are consistent, their spatial patterns are different as it can be seen in Figure 3. It is also worth mentioning that USDM does not strictly rely on SM percentiles for characterizing the drought conditions rather it uses streamflow and precipitation at different time scales, groundwater, local experts, etc.

Table 1. Drought and wetness extent correlations between USDM and different approaches.

	D0	D1	D2	D3	D4
DA_NLDAS, DA_IMERG	0.77	0.80	0.84	0.82	0.94
DA_NLDAS, USDM	0.86	0.83	0.80	0.71	0.55
DA_IMERG, USDM	0.77	0.82	0.79	0.76	0.64
	W0	**W1**	**W2**	**W3**	**W4**
DA_NLDAS, DA_IMERG	0.70	0.69	0.67	0.63	0.69

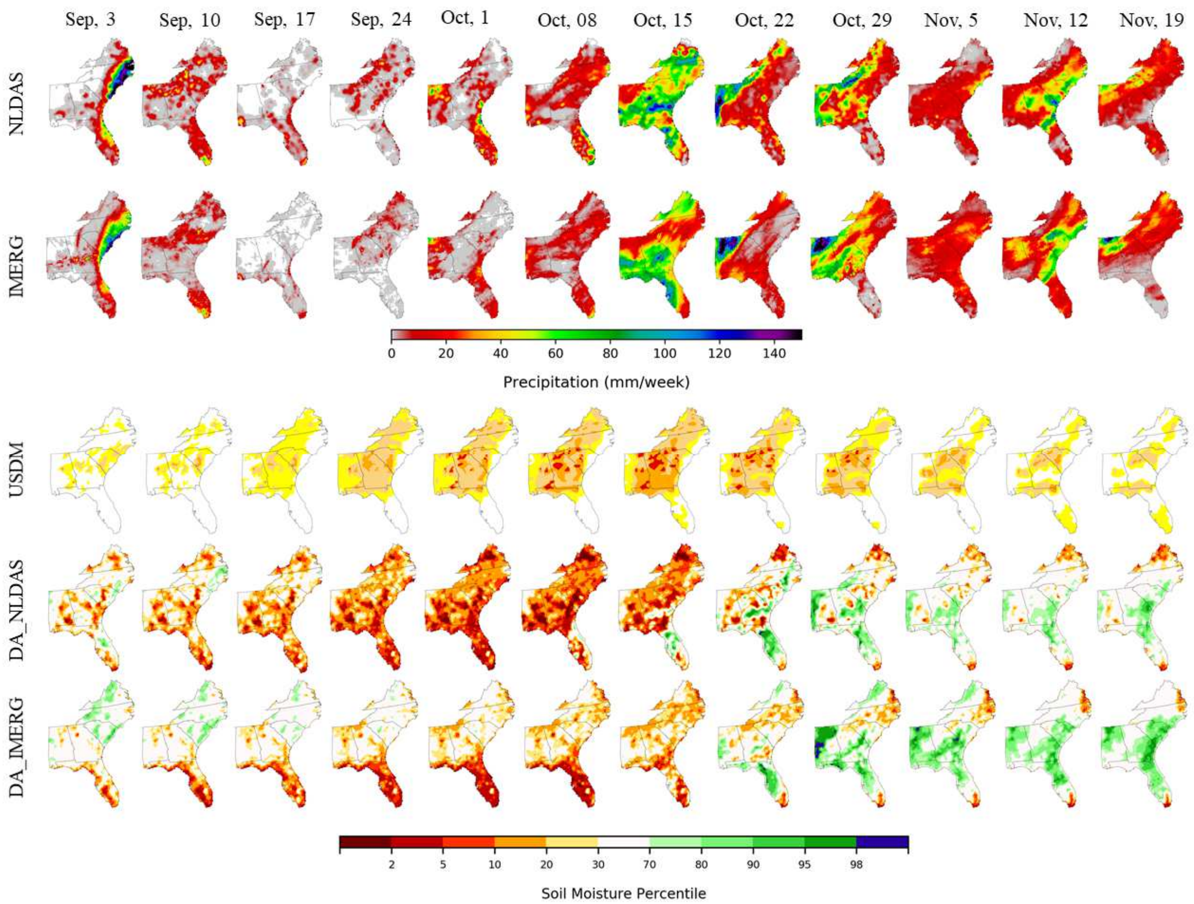

Figure 5. A demonstration of the flash drought evolution happened in the Southeast US in the Fall of 2019. It is worth mentioning that the day September 3rd shown in the first row means the weekly drought/precipitation conditions beginning on September 3, 2019, and ending on September 9, 2019 to be consistent with the USDM.

5.3 Fall 2019 flash drought

During September and early October 2019, a large portion of the Southeast US experienced extremely dry conditions which were characterized by record or near record-breaking precipitation deficit and extreme heat (NOAA, 2021c). D0-D3 drought conditions developed rapidly, growing from 25% (percentage of area under drought) at the beginning of September to 80% by the end of this month (Schubert et al., 2021). High-pressure air conditions hovered over this area for several weeks, bringing record-breaking temperatures, dry air, and low rates of precipitation (Weather, 2021). Alabama, Florida, and Georgia had their driest September on record over the 1895-2019 period and other states such as Virginia had the second driest (Schubert et al., 2021). The above-normal precipitation during the second half of October significantly alleviated the drought conditions, and by the end of November mostly normal and above-average wetness conditions were observed.

Hurricane Dorian made landfall in the first week of September and brought heavy rainfall over east and coastal areas of North Carolina and South Carolina and some locations in Florida. Both NLDAS and IMERG products depict this rainfall event with similar spatial patterns, although with different intensities. The drought maps provided by DA_NLDAS and DA_IMERG both report wet conditions, as expected, over the regions impacted by the heavy rainfall of Hurricane Dorian, while USDM shows an abnormally dry condition. In the USDM maps, these areas remain in normal conditions for the entire period, while DA_IMERG and DA_NLDAS report rapid dry conditions starting from the week of September, 24 to mid-October. It is also important to note that, in general, DA_IMERG is showing a wetter condition compared to the DA_NLDAS and USDM maps. In our previous study (Gavahi et al., 2020), we had investigated the USDM drought maps during the period of Hurricane Micheal and compared those with the ones developed by our hydrologic data assimilation system over the ACF (Apalachicola-Chattahoochee-Flint) region. The results showed that the USDM had one week lag in responding to heavy rainfall from Hurricane Micheal. The same pattern is also discernible for this flash drought event. Heavy precipitation occurs in the week of October, 15th based on both NLDAS and IMERG. It can be seen that in the following week, both DA_NLDAS and DA_IMERG are showing above normal and wet conditions compared to the USDM whose drought maps remained unchanged. IMERG and NLDAS show different precipitation patterns over northwest Alabama (see October 22 in Figure 5), and the same discrepancies can be observed from the corresponding drought maps. This further implies the significance of precipitation data in driving the LSM for drought monitoring.

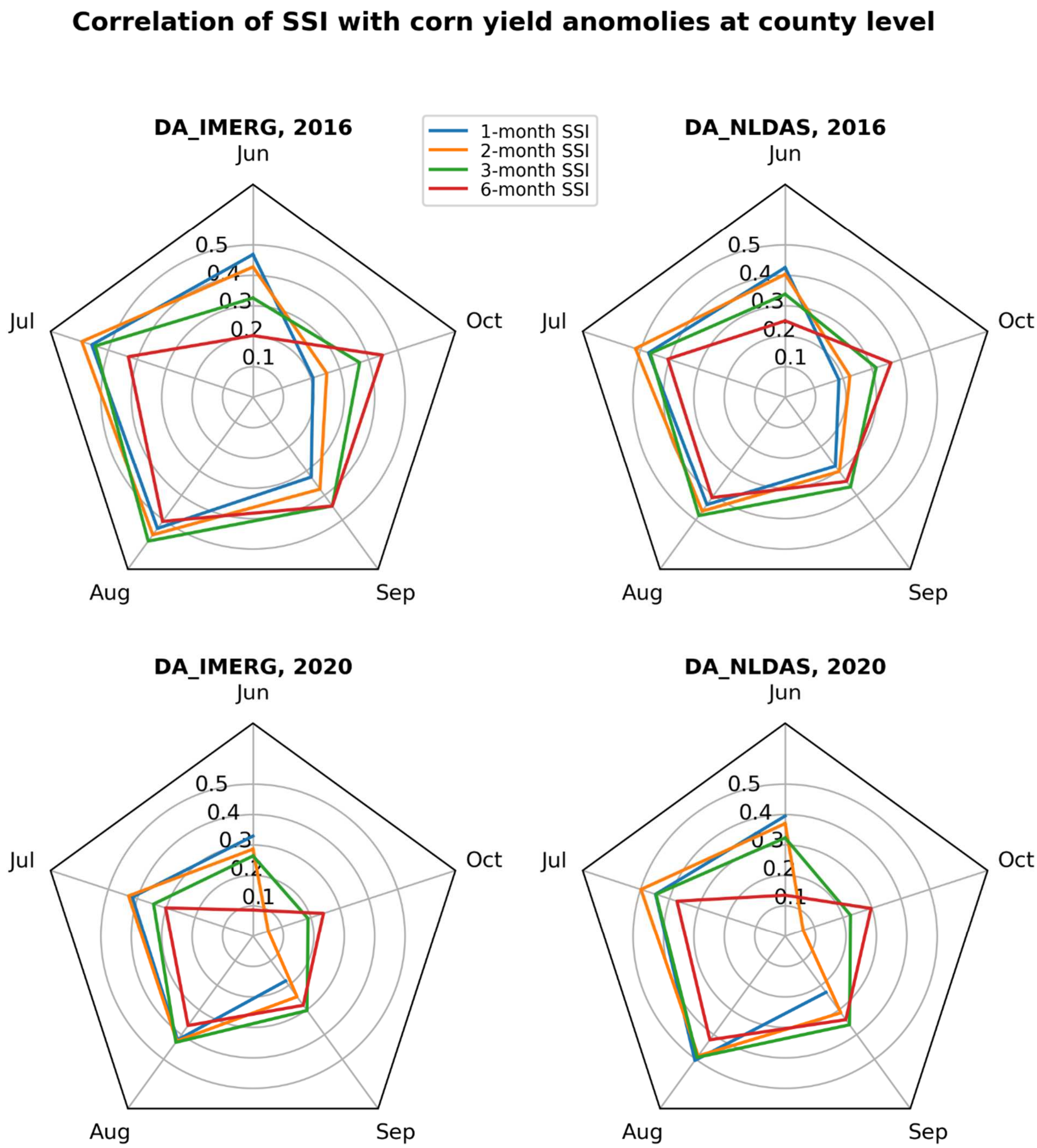

Figure 6. Comparison between DA_NLDAS and DA_IMERG SSI correlations with corn yield anomalies at the county level for years 2016 and 2020.

496

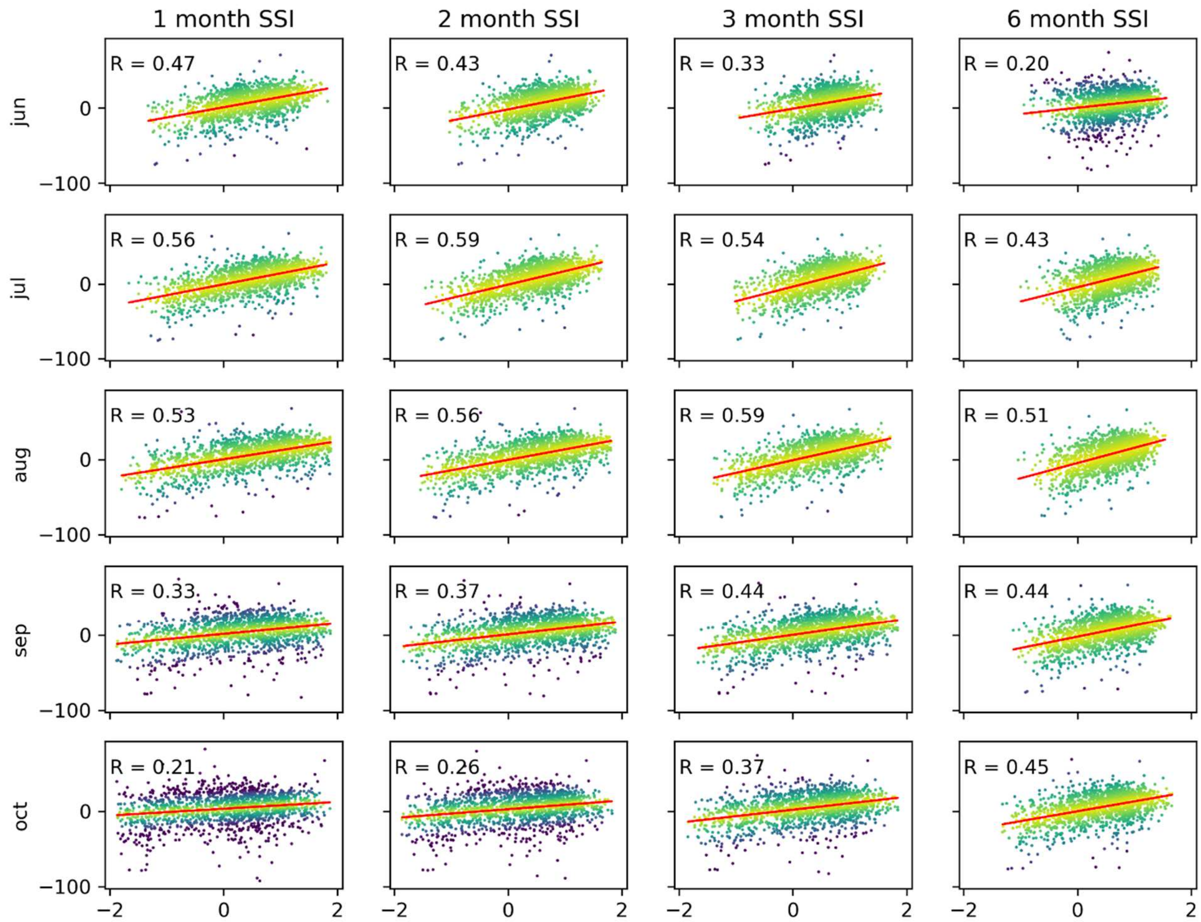

497 Figure 7. Scatter plots of DA_IMERG SSI versus corn yield anomalies at the county level in
498 2016 for different months during the plant growing season and for 1, 2, 3, and 6-month SSI.
499

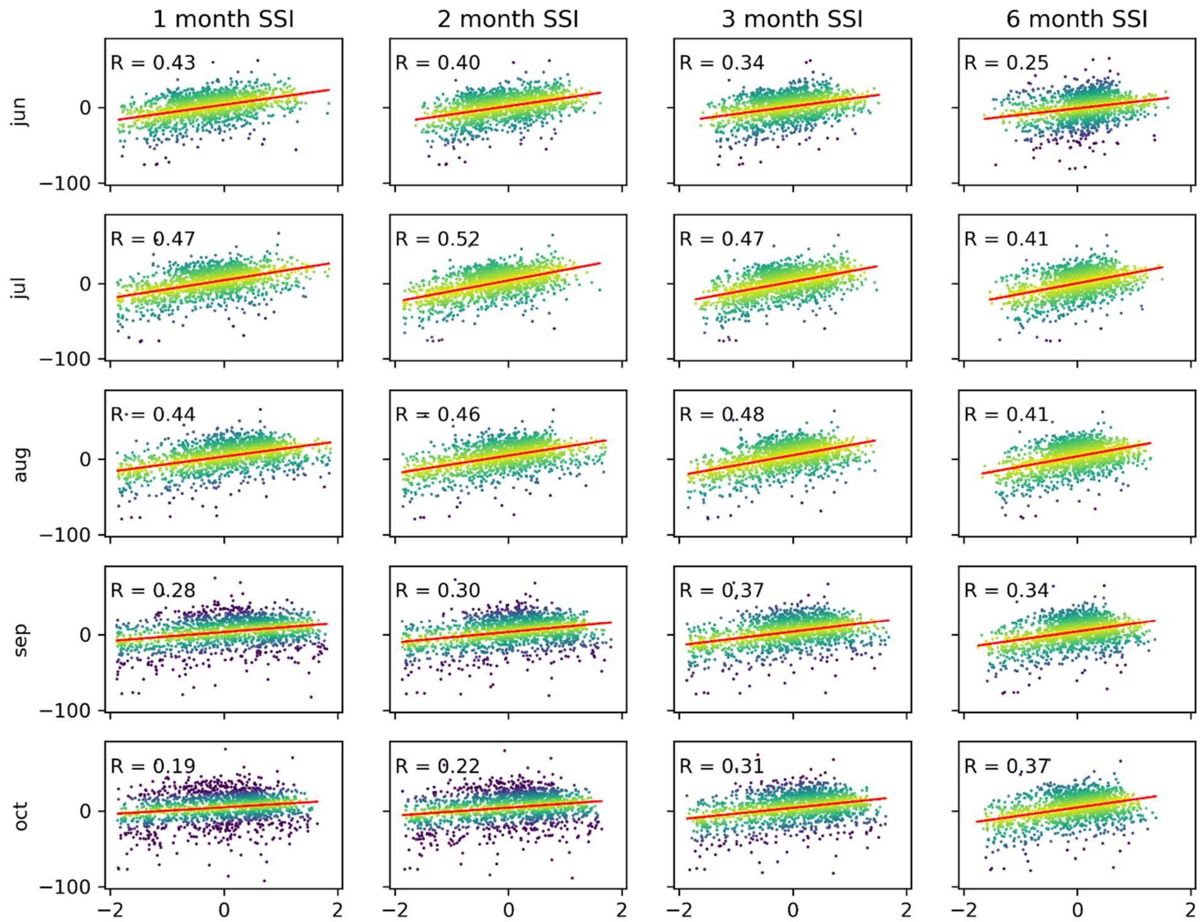

Figure 8. Same as figure 7 but for DA_NLDAS.

5.4 Corn yield analysis over the CONUS

Here, to provide a comprehensive analysis of the efficacy of produced drought maps, we investigated the impact of detected drought events on the corn yield over the corn belt and other major corn-producing states in the US (Gavahi et al., 2021). We calculated the county-based corn yield anomalies using the method provided in (Lu et al., 2017). It is also important to note that the reported results are based on spatial correlation at a given year. Figures 6-8 represent the correlation coefficient between the Standardized Soil Moisture Index (SSI) at different time scales (i.e., 1-month, 2-month, 3-month, and 6-month) and corn yield from June to October. We can see in all these figures the SSI is positively correlated with the corn yield anomaly indicating a direct relationship between the positive and negative SSI and the above and below normal yield values, respectively. The highest correlation rates can be observed for 2-month SSI in July, which is the two-month period that covers most of the growing season. In general, in 2016, DA_IMERG resulted in higher correlations compared to DA_NLDAS, however, in 2020, SSI derived from DA_NLDAS has had better agreement with the corn yield anomalies. Therefore, it can be concluded that depending on different forcing meteorological data, the drought events detected by the land data assimilation system may be differently correlated with the crop yield. The lowest correlation can be seen in 1-month SSI in October which is the end of harvesting season and drought has the lowest effect on the crop yield. We noticed that as we move from 1-month to 6-month SSI, the correlations increase as the SSI is passing over the growing season. 2-month SSI in July and 3-month SSI in August are showing the highest correlation rates for both datasets as they are capturing the most critical period of the growing season.

Our analysis indicates that regardless of the precipitation forcing used in the land surface data assimilation system for drought monitoring, this modeling platform is able to effectively detect the drought events' impacts on crop yield. This can be attributed to multivariate assimilation of soil moisture and ET observations, which is consistent with the findings of other studies (e.g., Rigden et al., 2020) that concluded the importance of jointly considering these hydrologic variables for predicting crop yield. In this study, we also noticed that the produced agricultural drought maps better represent the corn yield anomalies compared to other crops such as soybean and vegetables. This is most likely due to the rooting depth of the corn (0.9 m, (FAO, 2021)) which is consistent with the depth of the soil profile of the LSM from which the soil moisture is estimated. However, the rooting depth of the soybean and vegetables are around 0.6 m and 0.4 m (FAO, 2021) that falls within the layers above the model's root zone depth considered in this study for agricultural drought monitoring. For reasonable analysis, the soil depth for which the soil moisture is estimated should be consistent with the rooting depth of the cultivar which is being studied. As it is seen from the above figures, there are some locations where the SSI is very low (indicating severe drought) while the yield anomaly is still above normal. This may be related to agricultural practices and irrigation management which may vary for each location resulting in different drought resilience abilities (Engström et al., 2020).

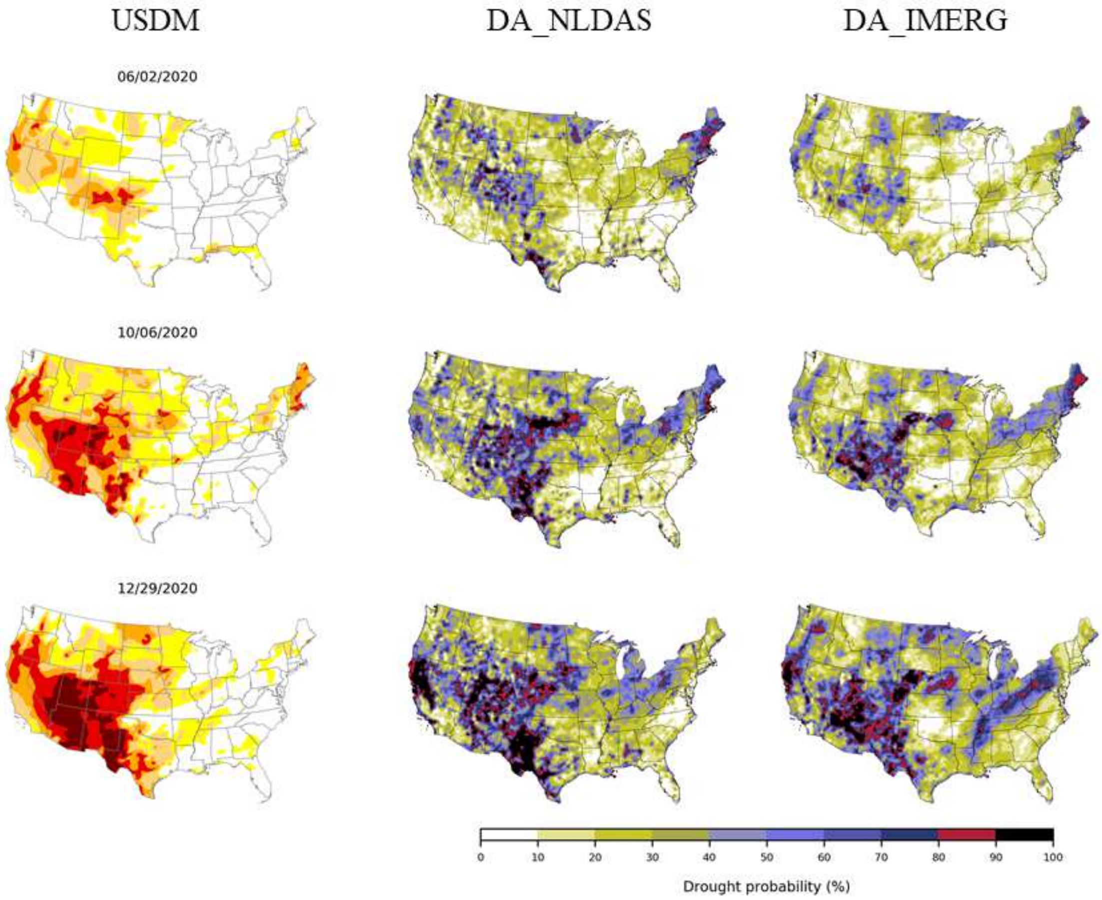

Figure 9. Probabilistic drought maps for the D0 drought category for three specific weeks in the year 2020.

5.5 Impacts on probabilistic drought maps

Uncertainty and accuracy of drought monitoring systems in identifying the drought onset, duration, and termination are of utmost importance for decision-makers, stakeholders, and managers to assess the risk associated with future drought events. This is achievable via land surface data assimilation systems that provide a reliable platform for probabilistic drought monitoring. Unlike other studies that mostly represented drought conditions in a deterministic way (Jiao et al., 2019b, 2019a; Mishra et al., 2017; Sadri et al., 2018; Son et al., 2021), here we utilized our drought monitoring system based on satellite data assimilation to provide probabilistic drought maps. These products are compared with drought maps available from USDM for three weeks of June, October, and December of 2020 in Figure 9. We calculated the drought probability based on the ensemble of soil moisture percentiles and their corresponding CDFs. In this figure, for example, the red color shows the areas with an 80-90 percent probability of experiencing D0 (abnormally dry condition) or more severe drought conditions. This figure highlights the contribution of different precipitation data (NLDAS and IMERG) in improving the drought monitoring skill of the Noah-MP LSM. In December 2020, DA_NLDAS shows a higher drought probability compared to DA_IMERG over California, where the USDM shows moderate to severe drought conditions. DA_IMERG resulted in a higher drought probability compared to DA_NLDAS in northern high plains, where the USDM reported abnormal to severe drought conditions. Higher drought categories in the USDM map are associated with higher probabilities in both DA_IMERG and DA_NLDAS maps.

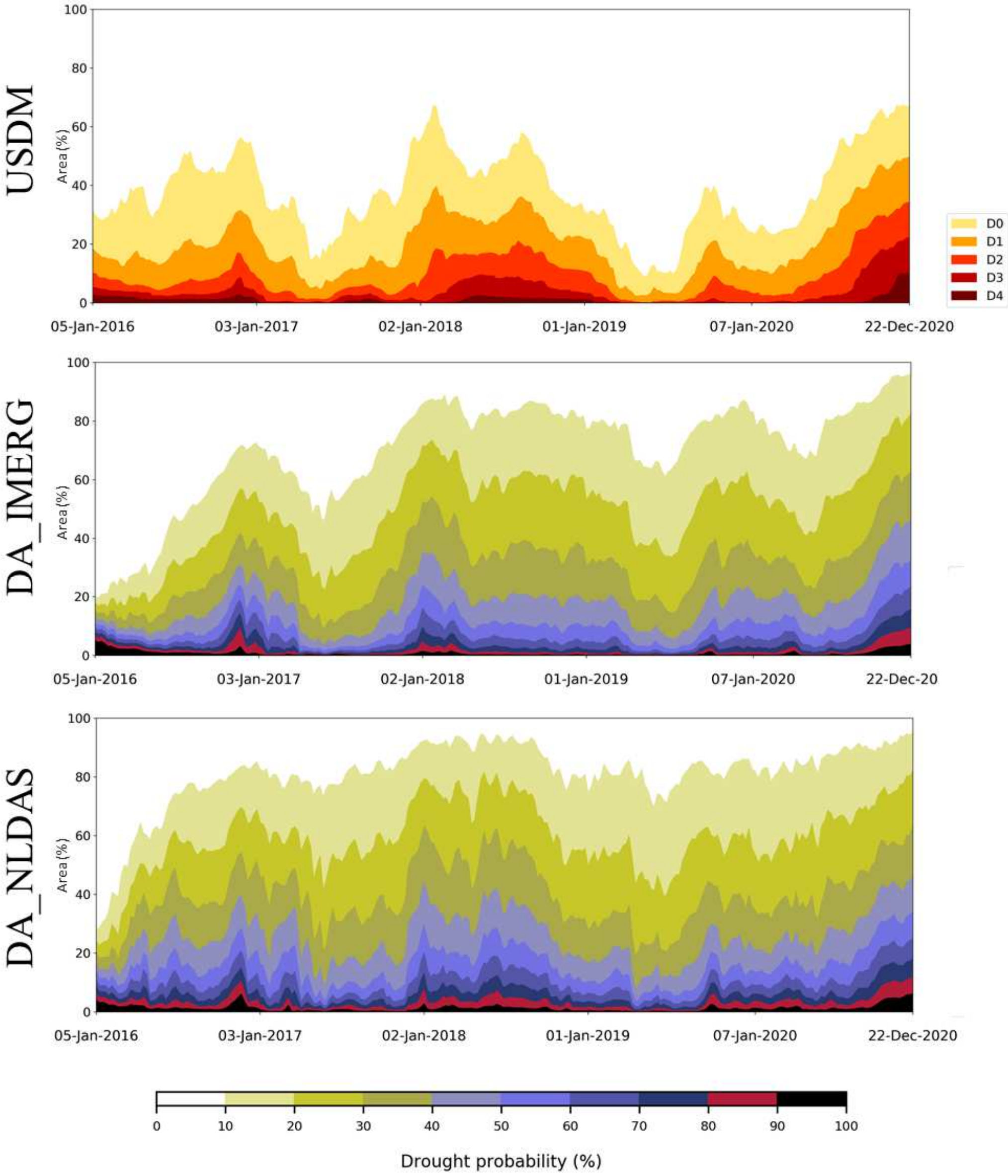

Figure 10. Probabilistic drought extent over the CONUS for the D0 category and a comparison with USDM. For the USDM map, the drought extents for categories D1-D4 are also presented.

Figure 10 represents the probabilistic temporal dynamics of D0 drought areal extent from DA_IMERG and DA_NLDAS products compared to the USDM deterministic drought extent categories. To develop this figure, we calculated the percentage of area under the D0 drought condition associated with each probability interval. When comparing DA_IMERG and

DA_NLDAS, we observe that at higher probabilities these two products represent similar drought coverage, however, as we move toward lower probabilities their temporal patterns get more deviated. More severe drought conditions reported by the USDM correspond to higher probabilities (>70 percent) of the D0 drought category regardless of the type of precipitation forcing data. Looking at the spatial pattern of drought probabilities for different categories in Figure 11 shows that the higher the severity of drought the lower the probability. We investigated this by analyzing drought probabilities in two different weeks during the summer and winter of 2020. DA_NLDAS and DA_IMERG similarly represent the spatial pattern of drought probabilities across different categories, however, their temporal variations as discussed in Figure 10 are slightly different. The higher probability of D0 abnormally dry condition over the western US during winter 2020 is in agreement with the mega-drought reported by USDM and NOAA report. This implies the usefulness of our developed land surface data assimilation system in probabilistically representing the drought conditions over the CONUS.

This analysis can be performed at regional or local scales to help in efficient agricultural management and irrigation scheduling. Depending on the sensitivity of each cultivar to a certain drought category, the associated probability can be used to see the effectiveness of the adopted strategy. Furthermore, this product can be useful for assessing the risk associated with each drought condition and developing agricultural disaster mitigation measures. In addition, our study signifies the importance of taking into account the uncertainty associated with the atmospheric forcing such as precipitation in understanding the future spatiotemporal variations of drought under climate change.

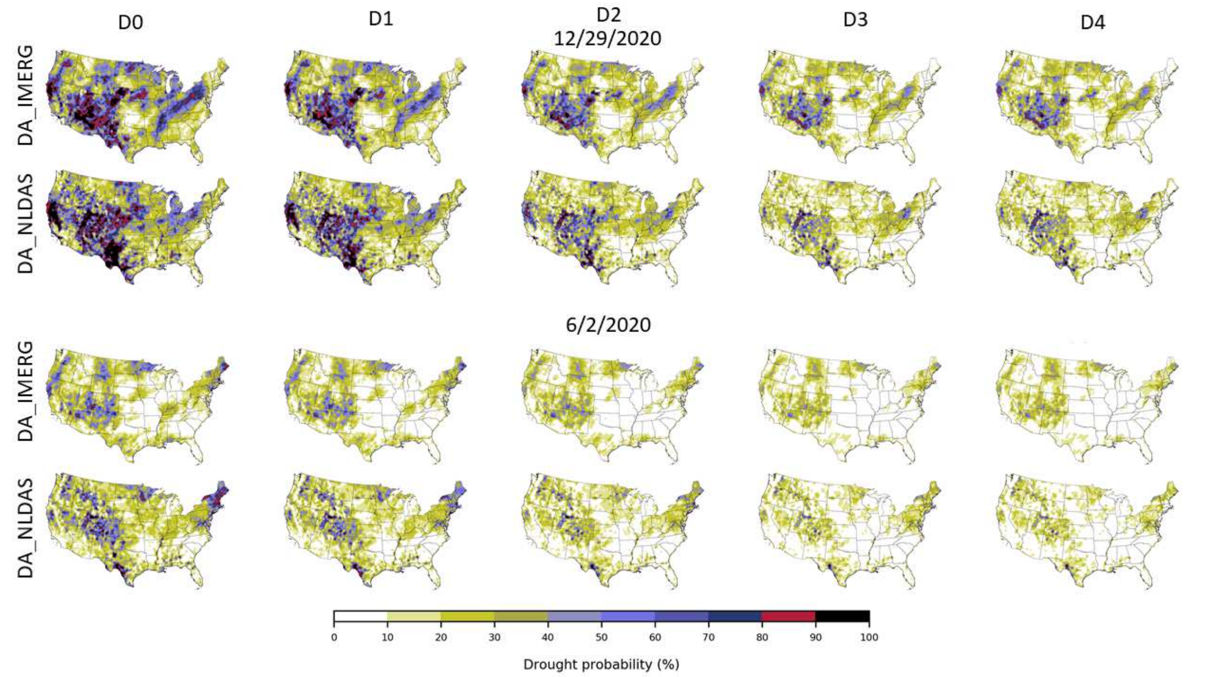

Figure 11. A comparison between DA_IMERG and DA_NLDAS probabilistic drought maps for various drought categories and for two different dates.

6. Summary and Conclusion

In this study, we comprehensively investigated the suitability of two different precipitation products, namely the NLDAS and IMERG, as inputs to a multivariate data assimilation framework that uses Noah-MP as its LSM and examined the impacts on different applications such as crop yield loss, flash droughts, and probability drought maps over the CONUS. We used the fully parallelized divide-and-conquer multivariate evolutionary particle filter algorithm as the data assimilation framework where SM and ET are simultaneously assimilated into the Noah-MP model for more accurate and reliable SM estimations. Later, we used the soil moisture estimates and compared them with the climatology of the SM from 2000 to 2020 to calculate the SM percentiles and develop drought maps over the CONUS having both NLDAS and IMERG as precipitation forcings. A comparison with the USDM maps showed that DA_NLDAS and

DA_IMERG are relatively consistent with the USDM drought maps although some discrepancies were also shown. The results also showed significant differences between DA_NLDAS and DA_IMERG drought maps over various regions which shows the significance of forcing precipitation data uncertainty that can greatly affect drought representation. A comparison between DA_NLDAS and DA_IMERG during the flash drought of the Southeast US in Fall 2019, showed that overall, DA_IMERG is showing wetter conditions as compared to DA_NLDAS and USDM. Furthermore, we observed that the USDM map responded with one week latency to Hurricane Dorian that made landfall in the first week of September and resulted in the termination of flash drought.

To provide a comprehensive analysis of the efficacy of the produced drought maps, we investigated the impact of detected drought events on the corn yield over the corn belt and other major corn-producing states in the US. Our analysis indicates that regardless of the precipitation forcing data product used in the land surface data assimilation system for drought monitoring, our modeling framework can effectively detect the drought impacts on crop yield.

Additionally, we calculated the drought probability based on the ensemble of soil moisture percentiles and their corresponding CDFs to develop probabilistic drought maps based on both NLDAS and IMERG as precipitation drivers and compared them with the USDM. The findings of this study showed that there exists temporal and spatial discrepancies in drought probability maps generated from NLDAS and IMERG precipitation forcing. Especially, as we move towards lower probabilities their temporal patterns get more deviated. The results also showed that higher drought categories in the USDM map are associated with higher probabilities in both DA_IMERG and DA_NLDAS maps. Finally, the higher probability of D0 abnormally dry condition over the western US during winter 2020 is in agreement with the mega-drought reported by the USDM and NOAA reports which shows the effectiveness of our developed land surface data assimilation system in probabilistically representing the drought conditions over the CONUS.

This study shows the importance of the precipitation dataset used for the task of drought monitoring, especially when land data assimilation is used. The findings of this study revealed that the inherent spatiotemporal uncertainties in the precipitation forcing data used can have a significant impact on the results and the drought maps generated. Hence, it is important to take into account the precipitation forcing data uncertainties in our drought monitoring procedures and analyze drought impacts. For future research, it is worth providing an inter-comparison between various precipitation datasets and identifying their corresponding uncertainties by comparing them against in-situ stations and other precipitation measurements while quantifying the relations between inherent uncertainties and differences between drought conditions based on different precipitation datasets.

Acknowledgments

Partial financial support for this project was provided by the National Oceanic and Atmospheric Administration (NOAA) Modeling, Analysis, Predictions, and Projections (MAPP) (Grant NA18OAR4310319).

Data availability statement

All the datasets used in this study are publicly available and can be accessed through the mentioned links/citations provided throughout the text.

References

Abbaszadeh, P., Gavahi, K., Moradkhani, H., 2021a. Bayesian Multi-modeling of Deep Neural Nets for Probabilistic Crop Yield Prediction. Agric. For. Meteorol.

Abbaszadeh, P., Moradkhani, H., Daescu, D.N., 2019a. The Quest for Model Uncertainty Quantification: A Hybrid Ensemble and Variational Data Assimilation Framework. Water Resour. Res. 55, 2407–2431. https://doi.org/10.1029/2018WR023629

Abbaszadeh, P., Moradkhani, H., Gavahi, K., Kumar, S., Hain, C., Zhan, X., Duan, Q., Peters-Lidard, C., Karimiziarani, M., 2021b. High-Resolution SMAP Satellite Soil Moisture Product: Exploring the Opportunities. Bull. Am. Meteorol. Soc. 1–15. https://doi.org/10.1175/bams-d-21-0016.1

Abbaszadeh, P., Moradkhani, H., Yan, H., 2018. Enhancing hydrologic data assimilation by evolutionary Particle Filter and Markov Chain Monte Carlo. Adv. Water Resour. 111, 192–204. https://doi.org/10.1016/j.advwatres.2017.11.011

Abbaszadeh, P., Moradkhani, H., Zhan, X., 2019b. Downscaling SMAP Radiometer Soil Moisture Over the CONUS Using an Ensemble Learning Method. Water Resour. Res. 55, 324–344. https://doi.org/10.1029/2018WR023354

Araneda-Cabrera, R.J., Bermúdez, M., Puertas, J., 2021. Benchmarking of drought and climate indices for agricultural drought monitoring in Argentina. Sci. Total Environ. 790, 148090. https://doi.org/10.1016/J.SCITOTENV.2021.148090

Baniya, B., Tang, Q., Xu, X., Haile, G.G., Chhipi-Shrestha, G., 2019. Spatial and temporal variation of drought based on satellite derived vegetation condition index in Nepal from 1982–2015. Sensors (Switzerland) 19. https://doi.org/10.3390/S19020430

Barbu, A.L., Calvet, J.C., Mahfouf, J.F., Lafont, S., 2014. Integrating ASCAT surface soil moisture and GEOV1 leaf area index into the SURFEX modelling platform: A land data assimilation application over France. Hydrol. Earth Syst. Sci. 18, 173–192. https://doi.org/10.5194/hess-18-173-2014

Cai, X., Yang, Z.L., David, C.H., Niu, G.Y., Rodell, M., 2014. Hydrological evaluation of the Noah-MP land surface model for the Mississippi River Basin. J. Geophys. Res. Atmos. 119, 23–38. https://doi.org/10.1002/2013JD020792

Chen, X., Li, Y., Yao, N., Liu, D.L., Javed, T., Liu, C., Liu, F., 2020. Impacts of multi-timescale SPEI and SMDI variations on winter wheat yields. Agric. Syst. 185. https://doi.org/10.1016/J.AGSY.2020.102955

Cheng, S., Argaud, J.-P., Iooss, B., Lucor, D., Ponçot, A., 2020. Error covariance tuning in variational data assimilation: application to an operating hydrological model. Stoch. Environ. Res. Risk Assess. 2020 355 35, 1019–1038. https://doi.org/10.1007/S00477-020-01933-7

Cook, E.R., Seager, R., Cane, M.A., Stahle, D.W., 2007. North American drought: Reconstructions, causes, and consequences. Earth-Science Rev. 81, 93–134. https://doi.org/10.1016/J.EARSCIREV.2006.12.002

Cosgrove, B.A., Lohmann, D., Mitchell, K.E., Houser, P.R., Wood, E.F., Schaake, J.C., Robock, A., Sheffield, J., Duan, Q., Luo, L., Higgins, R.W., Pinker, R.T., Tarpley, J.D., 2003. Land surface model spin-up behavior in the North American Land Data Assimilation System (NLDAS). J. Geophys. Res. Atmos. 108, 8845. https://doi.org/10.1029/2002JD003316

CPC, 2021. w.rank.202012.gif (800×618) [WWW Document]. URL https://www.cpc.ncep.noaa.gov/products/Soilmst_Monitoring/Figures/monthly/w.rank.202012.gif (accessed 11.10.21).

Das, N.N., Entekhabi, D., Dunbar, R.S., Colliander, A., Chen, F., Crow, W., Jackson, T.J., Berg, A., Bosch, D.D., Caldwell, T., Cosh, M.H., Collins, C.H., Lopez-Baeza, E., Moghaddam, M., Rowlandson, T., Starks, P.J., Thibeault, M., Walker, J.P., Wu, X., O'Neill, P.E., Yueh, S., Njoku, E.G., 2018. The SMAP mission combined active-passive soil moisture product at 9 km and 3 km spatial resolutions. Remote Sens. Environ. 211, 204–217. https://doi.org/10.1016/j.rse.2018.04.011

Engström, J., Jafarzadegan, K., Moradkhani, H., 2020. Drought Vulnerability in the United States: An Integrated Assessment. Water 2020, Vol. 12, Page 2033 12, 2033. https://doi.org/10.3390/W12072033

FAO, 2021. Scaling soil nutrient balances [WWW Document]. URL https://www.fao.org/3/y5749e/y5749e0j.htm (accessed 11.10.21).

FEMA, 1995. National mitigation strategy: Partnerships for building safer communities [WWW Document]. Mitig. Dir. URL https://scholar.google.com/scholar?q=FEMA, 1995. National mitigation strategy: partnerships for building safer communities. Federal Emergency Management Agency, Washington, DC. (accessed 11.2.21).

Gavahi, K., Abbaszadeh, P., Moradkhani, H., 2021. DeepYield : A combined convolutional neural network with long short-term memory for crop yield forecasting. Expert Syst. Appl. 184, 115511. https://doi.org/10.1016/j.eswa.2021.115511

Gavahi, K., Abbaszadeh, P., Moradkhani, H., Zhan, X., Hain, C., 2020. Multivariate Assimilation of Remotely Sensed Soil Moisture and Evapotranspiration for Drought Monitoring. J. Hydrometeorol. 21, 2293–2308. https://doi.org/10.1175/jhm-d-20-0057.1

Guilloteau, C., Foufoula-Georgiou, E., Kirstetter, P., Tan, J., Huffman, G.J., 2021. How Well Do Multisatellite Products Capture the Space–Time Dynamics of Precipitation? Part I: Five Products Assessed via a Wavenumber–Frequency Decomposition. J. Hydrometeorol. 22, 2805–2823. https://doi.org/10.1175/JHM-D-21-0075.1

Hain, C.R., Crow, W.T., Anderson, M.C., Mecikalski, J.R., 2012. An ensemble Kalman filter dual assimilation of thermal infrared and microwave satellite observations of soil moisture into the Noah land surface model. Water Resour. Res. 48. https://doi.org/10.1029/2011WR011268

Hazra, A., Maggioni, V., Houser, P., Antil, H., Noonan, M., 2019. A Monte Carlo-based multi-objective optimization approach to merge different precipitation estimates for land surface modeling. J. Hydrol. 570, 454–462. https://doi.org/10.1016/J.JHYDROL.2018.12.039

Heim, R., 2002. A Review of Twentieth-Century Drought Indices Used in the United States.

Bull. Am. Meteorol. Soc. 83, 1149–1166. https://doi.org/10.1175/1520-0477-83.8.1149

Hong, Y., Hsu, K.L., Sorooshian, S., Gao, X., 2004. Precipitation Estimation from Remotely Sensed Imagery Using an Artificial Neural Network Cloud Classification System. J. Appl. Meteorol. Climatol. 43, 1834–1853. https://doi.org/10.1175/JAM2173.1

Hossain, F., Anagnostou, E.N., 2005. Numerical investigation of the impact of uncertainties in satellite rainfall estimation and land surface model parameters on simulation of soil moisture. Adv. Water Resour. 28, 1336–1350. https://doi.org/10.1016/J.ADVWATRES.2005.03.013

Huang, M., Wang, X., Keenan, T.F., Piao, S., 2018. Drought timing influences the legacy of tree growth recovery. Glob. Chang. Biol. 24, 3546–3559. https://doi.org/10.1111/GCB.14294

Javed, T., Li, Y., Rashid, S., Li, F., Hu, Q., Feng, H., Chen, X., Ahmad, S., Liu, F., Pulatov, B., 2021. Performance and relationship of four different agricultural drought indices for drought monitoring in China's mainland using remote sensing data. Sci. Total Environ. 759, 143530. https://doi.org/10.1016/J.SCITOTENV.2020.143530

Jiao, W., Tian, C., Chang, Q., Novick, K.A., Wang, L., 2019a. A new multi-sensor integrated index for drought monitoring. Agric. For. Meteorol. 268, 74–85. https://doi.org/10.1016/J.AGRFORMET.2019.01.008

Jiao, W., Wang, L., Novick, K.A., Chang, Q., 2019b. A new station-enabled multi-sensor integrated index for drought monitoring. J. Hydrol. 574, 169–180. https://doi.org/10.1016/J.JHYDROL.2019.04.037

Jin, C., Luo, X., Xiao, X., Dong, J., Li, X., Yang, J., Zhao, D., 2019. The 2012 Flash Drought Threatened US Midwest Agroecosystems. Chinese Geogr. Sci. 2019 295 29, 768–783. https://doi.org/10.1007/S11769-019-1066-7

Khaki, M., Hendricks Franssen, H.-J., Han, S.C., 2020. Multi-mission satellite remote sensing data for improving land hydrological models via data assimilation. Sci. Reports 2020 101 10, 1–23. https://doi.org/10.1038/s41598-020-75710-5

Kimwatu, D.M., Mundia, C.N., Makokha, G.O., 2021. Developing a new socio-economic drought index for monitoring drought proliferation: a case study of Upper Ewaso Ngiro River Basin in Kenya. Environ. Monit. Assess. 2021 1934 193, 1–22. https://doi.org/10.1007/S10661-021-08989-0

Koohi, S., Azizian, A., Brocca, L., 2021. Spatiotemporal drought monitoring using bottom-up precipitation dataset (SM2RAIN-ASCAT) over different regions of Iran. Sci. Total Environ. 779, 146535. https://doi.org/10.1016/J.SCITOTENV.2021.146535

Kumar, S. V., Peters-Lidard, C.D., Mocko, D., Reichle, R., Liu, Y., Arsenault, K.R., Xia, Y., Ek, M., Riggs, G., Livneh, B., Cosh, M., 2014. Assimilation of remotely sensed soil moisture and snow depth retrievals for drought estimation. J. Hydrometeorol. 15, 2446–2469. https://doi.org/10.1175/JHM-D-13-0132.1

Lai, C., Zhong, R., Wang, Z., Wu, X., Chen, X., Wang, P., Lian, Y., 2019. Monitoring hydrological drought using long-term satellite-based precipitation data. Sci. Total Environ. 649, 1198–1208. https://doi.org/10.1016/J.SCITOTENV.2018.08.245

Liu, L., Yang, X., Zhou, H., Liu, S., Zhou, L., Li, X., Yang, J., Han, X., Wu, J., 2018. Evaluating the utility of solar-induced chlorophyll fluorescence for drought monitoring by comparison with NDVI derived from wheat canopy. Sci. Total Environ. 625, 1208–1217. https://doi.org/10.1016/J.SCITOTENV.2017.12.268

Liu, Q., Zhang, S., Zhang, H., Bai, Y., Zhang, J., 2020. Monitoring drought using composite drought indices based on remote sensing. Sci. Total Environ. 711, 134585. https://doi.org/10.1016/J.SCITOTENV.2019.134585

Liu, X., Zhu, X., Pan, Y., Li, S., Liu, Y., Ma, Y., 2016. Agricultural drought monitoring: Progress, challenges, and prospects. J. Geogr. Sci. 2016 266 26, 750–767. https://doi.org/10.1007/S11442-016-1297-9

Lu, J., Carbone, G.J., Gao, P., 2017. Detrending crop yield data for spatial visualization of drought impacts in the United States, 1895–2014. Agric. For. Meteorol. 237–238, 196–208. https://doi.org/10.1016/J.AGRFORMET.2017.02.001

Mishra, A., Vu, T., Veettil, A.V., Entekhabi, D., 2017. Drought monitoring with soil moisture active passive (SMAP) measurements. J. Hydrol. 552, 620–632. https://doi.org/10.1016/j.jhydrol.2017.07.033

Moradkhani, H., Hsu, K.-L., Gupta, H., Sorooshian, S., 2005. Uncertainty assessment of hydrologic model states and parameters: Sequential data assimilation using the particle filter. Water Resour. Res. 41. https://doi.org/10.1029/2004WR003604

Moradkhani, H., Nearing, G., Abbaszadeh, P., Pathiraja, S., 2018. Fundamentals of Data Assimilation and Theoretical Advances, in: Handbook of Hydrometeorological Ensemble Forecasting. Springer Berlin Heidelberg, Berlin, Heidelberg, pp. 1–26. https://doi.org/10.1007/978-3-642-40457-3_30-1

Mu, Q., Heinsch, F.A., Zhao, M., Running, S.W., 2007. Development of a global evapotranspiration algorithm based on MODIS and global meteorology data. Remote Sens. Environ. 111, 519–536. https://doi.org/10.1016/j.rse.2007.04.015

Mu, Q., Zhao, M., Running, S.W., 2011. Improvements to a MODIS global terrestrial evapotranspiration algorithm. Remote Sens. Environ. 115, 1781–1800. https://doi.org/10.1016/j.rse.2011.02.019

NCDC, 2021a. uwa-vic-soil-moist-pct-200630.png (626×510) [WWW Document]. URL https://www.ncdc.noaa.gov/monitoring-content/sotc/drought/2020/06/uwa-vic-soil-moist-pct-200630.png (accessed 11.10.21).

NCDC, 2021b. noaa-nws-cpc-soil-moist-pct-jun20.gif (800×618) [WWW Document]. URL https://www.ncdc.noaa.gov/monitoring-content/sotc/drought/2020/06/noaa-nws-cpc-soil-moist-pct-jun20.gif (accessed 11.10.21).

NCDC, 2021c. noaa-nws-ncep-nldas-ensemble-soil-moist-pct-0703-30d.png (763×447) [WWW Document]. URL https://www.ncdc.noaa.gov/monitoring-content/sotc/drought/2020/06/noaa-nws-ncep-nldas-ensemble-soil-moist-pct-0703-30d.png (accessed 11.10.21).

NCDC, 2021d. usgs-groundwater-pct-us-0630.png (599×513) [WWW Document]. URL https://www.ncdc.noaa.gov/monitoring-content/sotc/drought/2020/06/usgs-groundwater-pct-us-0630.png (accessed 11.10.21).

NCDC, 2021e. GRACE_GWS_20200629.png (3300×2550) [WWW Document]. URL https://www.ncdc.noaa.gov/monitoring-content/sotc/drought/2020/06/GRACE_GWS_20200629.png (accessed 11.10.21).

NCDC, 2021f. EDDI_01mn_20200627.png (1024×1024) [WWW Document]. URL https://www.ncdc.noaa.gov/monitoring-content/sotc/drought/2020/06/EDDI_01mn_20200627.png (accessed 11.10.21).

NCDC, 2021g. ESI.us_esi4km_01mn_2020182ann.jpg (680×520) [WWW Document]. URL https://www.ncdc.noaa.gov/monitoring-content/sotc/drought/2020/06/ESI.us_esi4km_01mn_2020182ann.jpg (accessed 11.10.21).

NCDC, 2021h. SPoRT-LIS-soil-moist.vsm0-200percent_20200630_00z_conus.gif (1200×800) [WWW Document]. URL https://www.ncdc.noaa.gov/monitoring-content/sotc/drought/2020/06/SPoRT-LIS-soil-moist.vsm0-200percent_20200630_00z_conus.gif (accessed 11.10.21).

NCDC, 2021i. ucla-vic-soil-moist-pct-201031.png (616×506) [WWW Document]. URL https://www.ncdc.noaa.gov/monitoring-content/sotc/drought/2020/10/ucla-vic-soil-moist-pct-201031.png (accessed 11.10.21).

NCDC, 2021j. noaa-nws-cpc-soil-moist-pct-1031.gif (800×618) [WWW Document]. URL https://www.ncdc.noaa.gov/monitoring-content/sotc/drought/2020/10/noaa-nws-cpc-soil-moist-pct-1031.gif (accessed 11.10.21).

NCDC, 2021k. noaa-nws-ncep-nldas-ensemble-soil-moist-pct-1030.png (825×484) [WWW Document]. URL https://www.ncdc.noaa.gov/monitoring-content/sotc/drought/2020/10/noaa-nws-ncep-nldas-ensemble-soil-moist-pct-1030.png (accessed 11.10.21).

NCDC, 2021l. GRACE_RTZSM_20201102.png (3300×2550) [WWW Document]. URL https://www.ncdc.noaa.gov/monitoring-content/sotc/drought/2020/10/GRACE_RTZSM_20201102.png (accessed 11.10.21).

NCDC, 2021m. noaa-hprcc-tmp-dep-us-1231-01m.png (2200×1700) [WWW Document]. URL https://www.ncdc.noaa.gov/monitoring-content/sotc/drought/2020/12/noaa-hprcc-tmp-dep-us-1231-01m.png (accessed 11.10.21).

NCDC, 2021n. GRACE_RTZSM_20210201.png (3300×2550) [WWW Document]. URL https://www.ncdc.noaa.gov/monitoring-content/sotc/drought/2021/01/GRACE_RTZSM_20210201.png (accessed 11.10.21).

NCEI, 2020. Drought - October 2020 | National Centers for Environmental Information (NCEI) [WWW Document]. URL https://www.ncdc.noaa.gov/sotc/drought/202010 (accessed 1.21.22).

Nichol, J.E., Abbas, S., 2015. Integration of remote sensing datasets for local scale assessment and prediction of drought. Sci. Total Environ. 505, 503–507. https://doi.org/10.1016/J.SCITOTENV.2014.09.099

NIDIS, 2021. What Is NIDIS? | Drought.gov.

Nijssen, B., Shukla, S., Lin, C., Gao, H., Zhou, T., Ishottama, Sheffield, J., Wood, E.F., Lettenmaier, D.P., 2014. A prototype global drought information system based on multiple land surface models. J. Hydrometeorol. 15, 1661–1676. https://doi.org/10.1175/JHM-D-13-090.1

Niu, G.Y., Yang, Z.L., Mitchell, K.E., Chen, F., Ek, M.B., Barlage, M., Kumar, A., Manning, K., Niyogi, D., Rosero, E., Tewari, M., Xia, Y., 2011. The community Noah land surface model with multiparameterization options (Noah-MP): 1. Model description and evaluation with local-scale measurements. J. Geophys. Res. Atmos. 116, 12109. https://doi.org/10.1029/2010JD015139

NLDAS, 2021. GES DISC Dataset: NLDAS Primary Forcing Data L4 Hourly 0.125 x 0.125 degree V002 (NLDAS_FORA0125_H 002) [WWW Document]. URL https://disc.gsfc.nasa.gov/datasets/NLDAS_FORA0125_H_002/summary (accessed 11.9.21).

NOAA, 2021a. 2020 U.S. billion-dollar weather and climate disasters in historical context | NOAA Climate.gov [WWW Document]. URL https://www.climate.gov/disasters2020 (accessed 1.21.22).

NOAA, 2021b. National Climate Report - January 2020 | National Centers for Environmental Information (NCEI) [WWW Document]. URL https://www.ncdc.noaa.gov/sotc/national/202001 (accessed 11.10.21).

NOAA, 2021c. Flash drought engulfs the U.S. Southeast in September 2019 | NOAA Climate.gov [WWW Document]. URL https://www.climate.gov/news-features/event-tracker/flash-drought-engulfs-us-southeast-september-2019 (accessed 11.11.21).

Piazzi, G., Thirel, G., Perrin, C., Delaigue, O., 2021. Sequential Data Assimilation for Streamflow Forecasting: Assessing the Sensitivity to Uncertainties and Updated Variables of a Conceptual Hydrological Model at Basin Scale. Water Resour. Res. 57. https://doi.org/10.1029/2020WR028390

Rigden, A.J., Mueller, N.D., Holbrook, N.M., Pillai, N., Huybers, P., 2020. Combined influence of soil moisture and atmospheric evaporative demand is important for accurately predicting US maize yields. Nat. Food 2020 12 1, 127–133. https://doi.org/10.1038/s43016-020-0028-7

Sadri, S., Wood, E.F., Pan, M., 2018. Developing a drought-monitoring index for the contiguous US using SMAP. Hydrol. Earth Syst. Sci. 22, 6611–6626. https://doi.org/10.5194/HESS-22-6611-2018

Salamanca, F., Zhang, Y., Barlage, M., Chen, F., Mahalov, A., Miao, S., 2018. Evaluation of the WRF-Urban Modeling System Coupled to Noah and Noah-MP Land Surface Models Over a Semiarid Urban Environment. J. Geophys. Res. Atmos. 123, 2387–2408. https://doi.org/10.1002/2018JD028377

Sawada, Y., Koike, T., Walker, J.P., 2015. A land data assimilation system for simultaneous simulation of soil moisture and vegetation dynamics. J. Geophys. Res. 120, 5910–5930.

https://doi.org/10.1002/2014JD022895

Schubert, S.D., Chang, Y., Deangelis, A.M., Wang, H., Koster, R.D., 2021. On the Development and Demise of the Fall 2019 Southeast U.S. Flash Drought: Links to an Extreme Positive IOD. J. Clim. 34, 1701–1723. https://doi.org/10.1175/JCLI-D-20-0428.1

Scofield, R.A., Kuligowski, R.J., 2003. Status and outlook of operational satellite precipitation algorithms for extreme-precipitation events. Weather Forecast. 18, 1037–1051. https://doi.org/10.1175/1520-0434(2003)018<1037:SAOOOS>2.0.CO;2

Sheffield, J., Wood, E.F., Chaney, N., Guan, K., Sadri, S., Yuan, X., Olang, L., Amani, A., Ali, A., Demuth, S., Ogallo, L., 2014a. A drought monitoring and forecasting system for sub-sahara african water resources and food security. Bull. Am. Meteorol. Soc. 95, 861–882. https://doi.org/10.1175/BAMS-D-12-00124.1

Sheffield, J., Wood, E.F., Chaney, N., Guan, K., Sadri, S., Yuan, X., Olang, L., Amani, A., Ali, A., Demuth, S., Ogallo, L., 2014b. A drought monitoring and forecasting system for sub-sahara african water resources and food security. Bull. Am. Meteorol. Soc. 95, 861–882. https://doi.org/10.1175/BAMS-D-12-00124.1

Shrestha, A., Nair, A.S., Indu, J., 2020. Role of precipitation forcing on the uncertainty of land surface model simulated soil moisture estimates. J. Hydrol. 580, 124264. https://doi.org/10.1016/J.JHYDROL.2019.124264

Son, B., Park, Sumin, Im, J., Park, Seohui, Ke, Y., Quackenbush, L.J., 2021. A new drought monitoring approach: Vector Projection Analysis (VPA). Remote Sens. Environ. 252, 112145. https://doi.org/10.1016/J.RSE.2020.112145

Svoboda, M., LeComte, D., Hayes, M., Heim, R., Gleason, K., Angel, J., Rippey, B., Tinker, R., Palecki, M., Stooksbury, D., Miskus, D., Stephens, S., 2002. THE DROUGHT MONITOR. Bull. Am. Meteorol. Soc. 83, 1181–1190. https://doi.org/10.1175/1520-0477-83.8.1181

Tan, J., Huffman, G.J., Bolvin, D.T., Nelkin, E.J., 2019. IMERG V06: Changes to the Morphing Algorithm. J. Atmos. Ocean. Technol. 36, 2471–2482. https://doi.org/10.1175/JTECH-D-19-0114.1

Van Oldenborgh, G.J., Van Der Wiel, K., Sebastian, A., Singh, R., Arrighi, J., Otto, F., Haustein, K., Li, S., Vecchi, G., Cullen, H., 2017. Attribution of extreme rainfall from Hurricane Harvey, August 2017. Environ. Res. Lett. 12, 124009. https://doi.org/10.1088/1748-9326/AA9EF2

Vicente-Serrano, S.M., Beguería, S., López-Moreno, J.I., 2010. A multiscalar drought index sensitive to global warming: The standardized precipitation evapotranspiration index. J. Clim. 23, 1696–1718. https://doi.org/10.1175/2009JCLI2909.1

Weather, 2021. Fall Heat Wave Crushed All-Time October Records in 80 Cities in South and East | The Weather Channel - Articles from The Weather Channel | weather.com [WWW Document]. URL https://weather.com/forecast/regional/news/2019-10-03-october-record-heat-south-east-midwest (accessed 11.10.21).

Xia, Y., Mitchell, K., Ek, M., Sheffield, J., Cosgrove, B., Wood, E., Luo, L., Alonge, C., Wei, H., Meng, J., Livneh, B., Lettenmaier, D., Koren, V., Duan, Q., Mo, K., Fan, Y., Mocko, D.,

2012. Continental-scale water and energy flux analysis and validation for the North American Land Data Assimilation System project phase 2 (NLDAS-2): 1. Intercomparison and application of model products. J. Geophys. Res. Atmos. 117, 3109. https://doi.org/10.1029/2011JD016048

Xu, L., Abbaszadeh, P., Moradkhani, H., Chen, N., Zhang, X., 2020. Continental drought monitoring using satellite soil moisture, data assimilation and an integrated drought index. Remote Sens. Environ. 250, 112028. https://doi.org/10.1016/j.rse.2020.112028

Yuan, X., Wang, L., Wu, P., Ji, P., Sheffield, J., Zhang, M., 2019. Anthropogenic shift towards higher risk of flash drought over China. Nat. Commun. 2019 101 10, 1–8. https://doi.org/10.1038/s41467-019-12692-7

Zeng, J., Yuan, X., Ji, P., Shi, C., 2021. Effects of meteorological forcings and land surface model on soil moisture simulation over China. J. Hydrol. 603, 126978. https://doi.org/10.1016/J.JHYDROL.2021.126978

Zhan, X., Fang, L., Yin, J., Schull, M., Liu, J., Hain, C., Anderson, M., Kustas, W., Kalluri, S., 2021. Remote Sensing of Evapotranspiration for Global Drought Monitoring. Geophys. Monogr. 265, 29–46. https://doi.org/10.1002/9781119427339.CH2

Zhao, W., Sánchez, N., Lu, H., Li, A., 2018. A spatial downscaling approach for the SMAP passive surface soil moisture product using random forest regression. J. Hydrol. 563, 1009–1024. https://doi.org/10.1016/j.jhydrol.2018.06.081

Zhou, J., Wu, Z., Crow, W.T., Dong, J., He, H., 2020. Improving Spatial Patterns Prior to Land Surface Data Assimilation via Model Calibration Using SMAP Surface Soil Moisture Data. Water Resour. Res. 56, e2020WR027770. https://doi.org/10.1029/2020WR027770

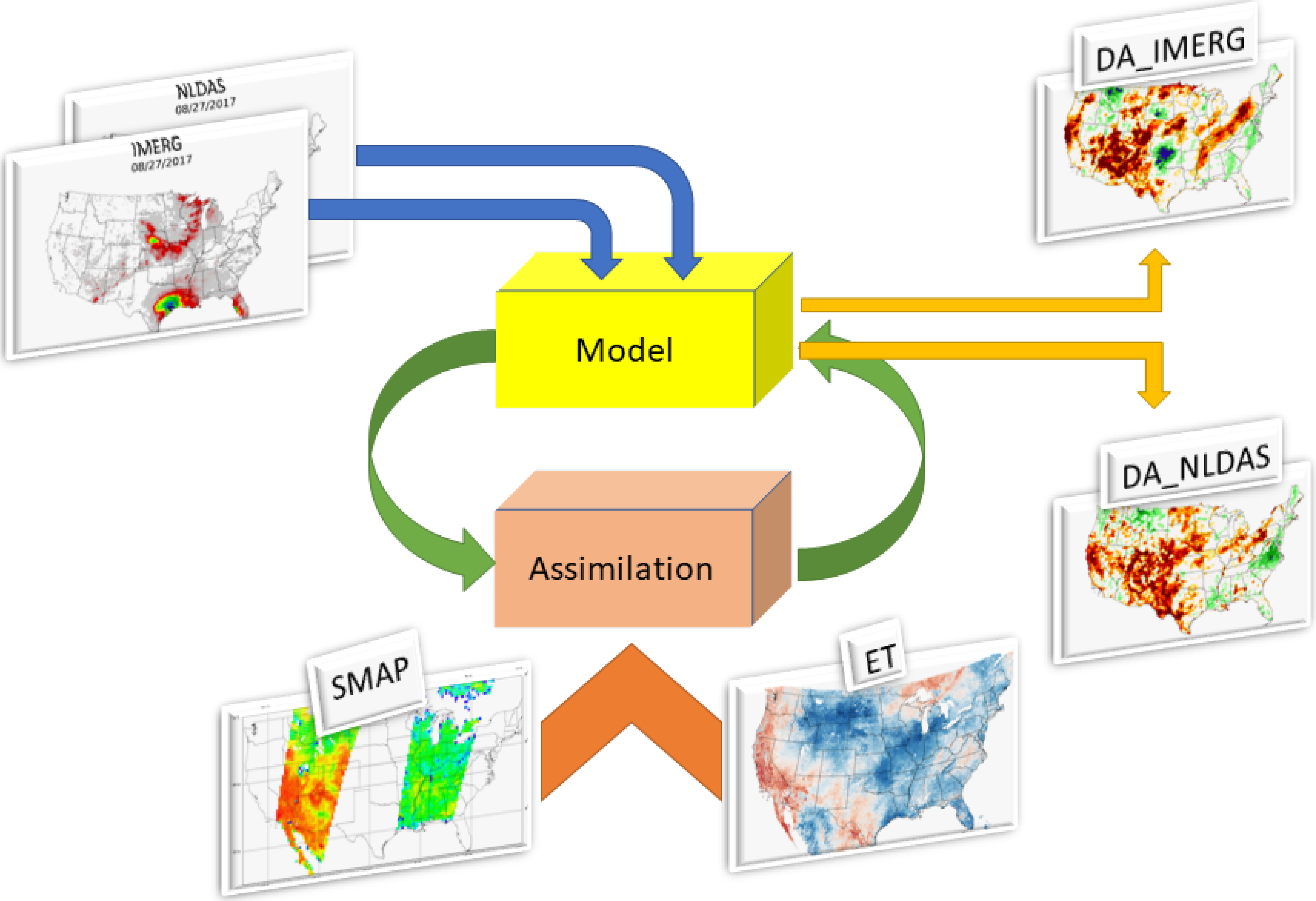
NLDAS
08/27/2017
IMERG
08/27/2017
Model
Assimilation
SMAP
ET
DA_IMERG
DA_NLDAS